Manipulating Nucleation Potency of Substrates by Interfacial Segregation

Subjects: Materials Science, Characterization & Testing

Contributor: Yun Wang, Shihao Wang, Zhongping Que, Changming Fang, Teruo Hashimoto, Xiaorong Zhou, Quentin M. Ramasse, Zhongyun Fan

During solidification of metallic materials, heterogeneous nucleation occurs on substrates, either endogenous or exogenous. The potency of the substrates for nucleation is mainly dependent upon the atomic arrangements on the substrate surface, which are affected by the lattice misfit between the substrate and the nucleated solid, the surface roughness at atomic scale, and the chemical interaction between the substrates and the melt. Extensive examinations on metal/substrate (M/S) interfaces at atomic scale by the state-of-the-art aberration (Cs) corrected STEM and associated EDS and EELS have shown that alloying elements in liquid melts tend to segregate at the interfaces, leading to the formation of various 2-dimensional compounds (2DCs) or 2-dimensional solutions (2DSs), depending upon segregation behavior of the elements. For instance, Al3Ti 2DC and Ti2Zr 2DC at the Al/TiB2 interface, Y2O3 2DC at the Mg/MgO interface, and a Si-rich 2DS layer at Al-Si/TiB2 interface have been identified. Such interfacial segregations significantly affect nucleation potency of the substrates, resulting in either promoting or impeding the heterogeneous nucleation process during solidification.

Keywords: interfacial segregation ; heterogeneous nucleation ; grain refinement

1. Introduction

A uniform solidification structure of fine and equiaxed grains is usually desirable for most engineering alloys, since it results in significant reduction of casting defects, leading to improved integrity and mechanical performance of the alloy castings [1][2][3][4][5]. Grain refinement of engineering alloys is usually achieved by inoculation through externally added grain refiners, which is common foundry practice in Al- and Mg- industries. The most widely used commercial grain refiners for Al alloys are Al-Ti-B based master alloys containing excess Ti (e.g., Al-3Ti-1B or Al-5Ti-1B), while Mg-Zr master alloy is the grain refiner commercially available for Mg alloys, although it is only effective for Al-free Mg alloys [3][6][7]. It has been well documented in the literature that promotion of the heterogeneous nucleation process by potent solid substrates, such as TiB_2 particles for Al- alloys and Zr for Mg- alloys, is an effective approach to achieving grain refinement, based on which a great deal of effort has been made over the last decades in the search for various particles potent for nucleation; yet, in spite of these efforts, there has only been success to some degree.

During solidification, heterogeneous nucleation occurs on solid substrates (either endogenous or exogenous particles) present in an alloy melt, and nucleation potency of the substrates is dependent on the atomic arrangement in their surface plane [8]. As one of the important factors determining the nucleating potency, the lattice misfit at the interface between a substrate and nucleated new solid phase can be greatly modified by altering the atomic configuration of the substrate surface. In addition, the recent studies revealed that substrate surface roughness at atomic level [9] and chemical interaction between the substrate and the melt [10] affect nucleation potency considerably. Modification of atomic configuration and chemistry of substrate surface has been found to result in significant changes in nucleation potency. A good example is that, instead of TiB_2 itself, an atomic layer of Al_3Ti 2-dimensional compound (2DC) on the (0 0 0 1) TiB_2 surface is actually responsible for the extremely high potency of the TiB_2 particles for nucleation of α-Al [11].

2. Segregation at Al/TiB_2 Interface

2.1. Nature of TiB_2 Particles

Figure 1a shows the morphology of TiB_2 particles in a commercial Al-5Ti-1B grain refiner master alloy, and **Figure 1**b is the statistical result of the particle size which fits a log-normal distribution with the size spreading over the range of 0.15 μm to 2.5 μm and with a geometrical mean of d_0 = 0.43 μm [12]. The faceted boride particles are typically of hexagonal shape, with the majority of the particles having a diameter/thickness ratio in the range of 3.1 to 5.6. The TEM image in

Figure 2a confirms that the TiB_2 particles are faceted with their {0 0 0 1} basal and {1 1 0 0} prismatic planes [11], as shown schematically in **Figure 2**b. It has been well documented in the literature that heterogeneous nucleation of Al occurs on the basal surface of TiB_2, where the (1 1 1)Al plane has the same hexagonal atomic arrangement to that of the basal plane of TiB_2.

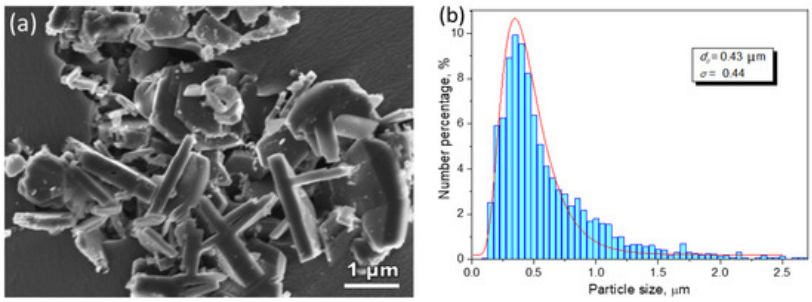

Figure 1. Nature of TiB_2 particles in commercial Al-5Ti-1B grain refiner [12]. (**a**) SEM image showing the typical hexagonal morphology; and (**b**) statistical analysis showing the log-normal size distribution with a geometrical mean of 0.43 μm and a standard deviation of 0.44. The grain refiner was supplied by LSM Co., Ltd.

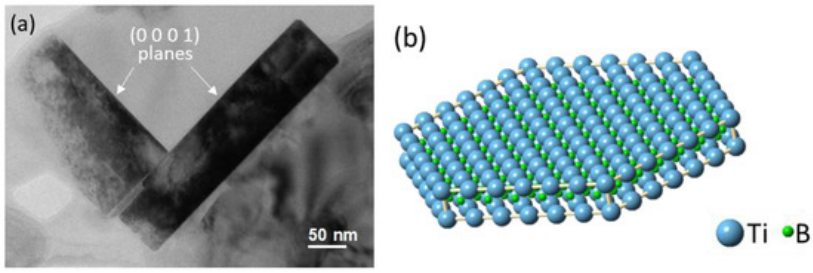

Figure 2. Surface termination and morphology of TiB_2 particles [11]. (**a**) TEM bright field image showing that the hexagonal TiB_2 particles are faceted with their {0 0 0 1} basal and {1 1 0 0} prismatic planes; and (**b**) 3D illustration showing schematically the atomic arrangement of TiB_2 crystal.

2.2. Al/TiB_2 Interface

Extensive TEM examination of multiple TiB_2 particles, which have clean surfaces without any elemental segregation, revealed that the majority of TiB_2 particles have no specific orientation relationship (OR) with the Al matrix. The high resolution TEM images in **Figure 3**a show an interface between Al and faceted (0 0 0 1) surface of a TiB_2 particle. It is seen that Al is away from any low index orientation while TiB_2 is in its [1 1 2¯ 0]

direction. Despite a low possibility, **Figure 3**b confirms that heterogeneous nucleation of Al does occur on theTiB_2 particle surface, where the $(1\ 1\ 1)_{Al}$ and $(0\ 0\ 0\ 1)_{TiB2}$ planes are paralleled to each other, with a deviation of 4.7 degrees between the $[0\ 1^{-}\ 1]_{Al}$ and $[1\ 1\ 2^{-}0]_{TiB2}$ directions. Therefore, the OR for "clean" (no interfacial segregation) TiB_2 and Al is:

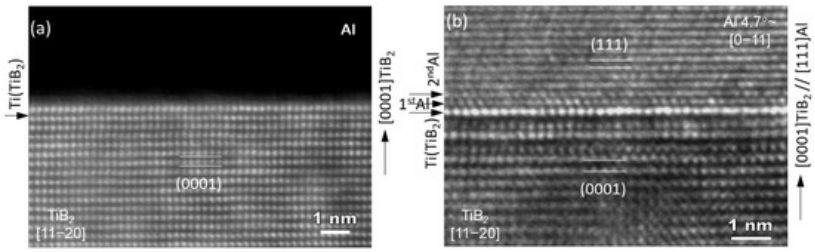

Figure 3. The interface between Al and a synthetic TiB_2 particle. HR-STEM images showing that (**a**) no particular orientation relationship (OR) between Al and TiB_2 and (**b**) (1 1 1)Al and (0 0 0 1)TiB_2 planes are paralleled to each other and a deviation of 4.7° between [0 1¯1]Al and [1 1 2¯ 0]TiB_2 directions [13]. The OR is: (0 0 0 1)TiB_2 // (1 1 1)Al, [1 1 2¯ 0]TiB_2 4.7°~ [0 1¯ 1]Al. However, there is no such deviation between the first Al layer (as indicated) and the TiB_2.

$$\begin{aligned} \mathrm{OR\,1:}\quad & (0\,0\,0\,1)_{\mathrm{Ti\,B_2}} \,//\, (1\,1\,1)_{\mathrm{Al}}, \\ & [1\,1\,\bar{2}\,0]_{\mathrm{Ti\,B_2}} \sim 4.7^{\circ} \ \text{off}\ [0\,\bar{1}\,1]_{\mathrm{Al}}. \end{aligned}$$

This is the direct experimental evidence to verify that clean a TiB_2 particle nucleates Al on its basal (0 0 0 1) surface. Theoretical work using molecular dynamics (MD) simulations by Fan et al. [13] recently demonstrated that, for a system with a negative lattice misfit, heterogeneous nucleation proceeds layer-by-layer, with the first layer accommodating the

misfit through an edge dislocation network; the second layer twisting an angle through a partial screw dislocation network to reduce lattice distortion; and the third layer creating a crystal plane of the solid (the 2D nucleus) that templates further growth. The experimental TEM observation in **Figure 3**b confirms the theoretical prediction that the −4.22% misfit between Al and TiB_2 requires such an orientational deviation, except for the first atomic layer for the TiB_2 templated Al nucleation, i.e., a twist of the nucleated solid relative to the substrate.

In the practice of inoculation to achieve grain refinement of Al alloys in industry, TiB_2 particles are introduced to the alloy melt by addition of commercial Al-5Ti-1B master alloy prior to solidification. Similar to the case in **Figure 3**a, the majority of the added TiB_2 particles show no specific OR with Al. However, well-defined OR was observed between the two crystals. As shown by the high-resolution TEM image in **Figure 4**a, the crystal planes of (1 1 1)Al and (0 0 0 1)TiB_2 are parallel to each other. Importantly, the directions of [0 1¯1]Al and [1 1 2¯ 0]TiB_2 are perfectly parallel to each other with no deviation, as indicated by the corresponding selected area electron diffraction (SAED) pattern in **Figure 4**b,c obtained from the area across the Al/TiB_2 interface. The OR for the TiB_2 from Al-5Ti-1B master alloy is thus identified as [11]:

$$\mathrm{OR\,2:}\ (0\,0\,0\,1)[1\,1\,\bar{2}\,0]_{\mathrm{Ti\,B_2}}\ //\ (1\,1\,1)[0\,\bar{1}\,1]_{\mathrm{Al}}$$

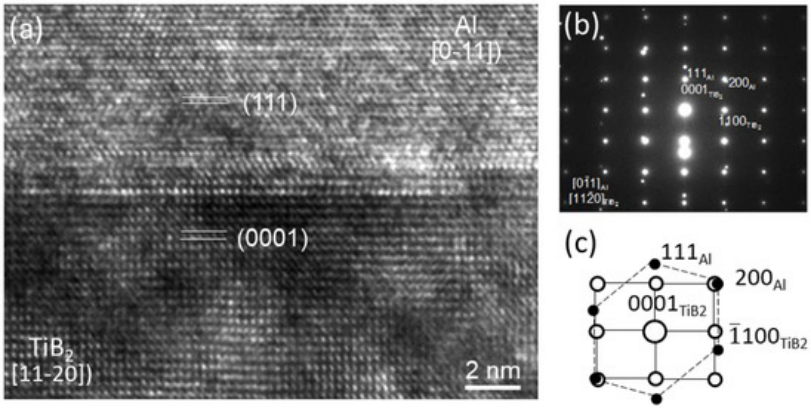

Figure 4. The interface between Al and TiB_2 from Al-5Ti-1B grain refiner [11]. (**a**) HR-TEM image showing the Al/TiB_2 interface viewed in the direction of [1 1 2¯0] TiB_2 and [0 1¯ 1]Al; (**b**) selected area electron diffraction (SAED) pattern taken from TiB_2 and Al across the interface; and (**c**) the indexed pattern of (**b**). The orientation relationship (OR) between TiB_2 and Al is: (0 0 0 1)[1 1 2¯ 0] TiB_2 // (1 1 1)[0 1¯1]Al.

By comparing **Figure 3**b and **Figure 4**, it is noted that there is no deviation between $[0\ 1\bar{1}1]_{Al}$ and $[1\ 1\ 2\bar{0}]_{TiB2}$ directions for the TiB_2 from the grain refiner. This is attributed to Ti segregation at the Al/TiB_2 interface, leading to a reduced lattice misfit between Al and TiB_2 at the interface [11][13], which is further discussed in the next section.

OR2 indicates that, at the Al/TiB_2 interface, the most densely packed crystal planes with a hexagonal atomic arrangement of TiB_2 and α-Al, i.e., $(0\ 0\ 0\ 1)_{TiB2}$ and $(1\ 1\ 1)_{\alpha\text{-Al}}$, are matching each other, with their most-densely packed directions, i.e., $[1\ 1\ 2\bar{0}]_{TiB2}$ and $[0\ 1\bar{1}1]_{\alpha\text{-Al}}$, being parallel to each other. The fact that the majority of TiB_2 particles were far away from any particular OR with α-Al indicates that most of the added boride particles did not contribute to the nucleation process, consistent with the conclusion derived from the free growth model, that only 0.1~1% of the added TiB_2 particles are active for heterogeneous nucleation [14].

Addition of Al-Ti-B grain refiners to Al alloy melts prior to solidification is a common practice in the Al industry, which gives castings a significant grain refinement with fully columnar-to-equiaxed transition (CET). As shown in **Figure 5**a,b, the grain structure of CP-Al solidified in the TP-1 mold changed dramatically from coarse columnar to fine equiaxed when 0.2% commercial Al-5Ti-1B grain refiner was added. The average size of α-Al grains achieved with the inoculation by TiB_2 was quantified as 175 ± 16 μm [11], indicating the powerful grain refining effect of the grain refiner. However, additions of synthetic TiB_2 particles (**Figure 5**c), or the synthetic particles plus 56 ppm excess Ti (**Figure 5**d), where the size distribution and number density of the added synthetic TiB_2 particles and the excess Ti concentration were equivalent to those of the addition of 0.2% Al-5Ti-1B [11], showed no grain refining effect. A coarse and columnar grain structure resulted, although the width of the columnar grains appeared finer than those of the sample without addition of the particles. This demonstrates that synthetic TiB_2 particles do not have the ability to grain refine α-Al, even combined with access to Ti in the melt [11]. The result from grain refinement tests and the absence of deviation in OR2 suggest that there is something different between the synthetic TiB_2 and those from the commercial Al-5Ti-1B grain refiner.

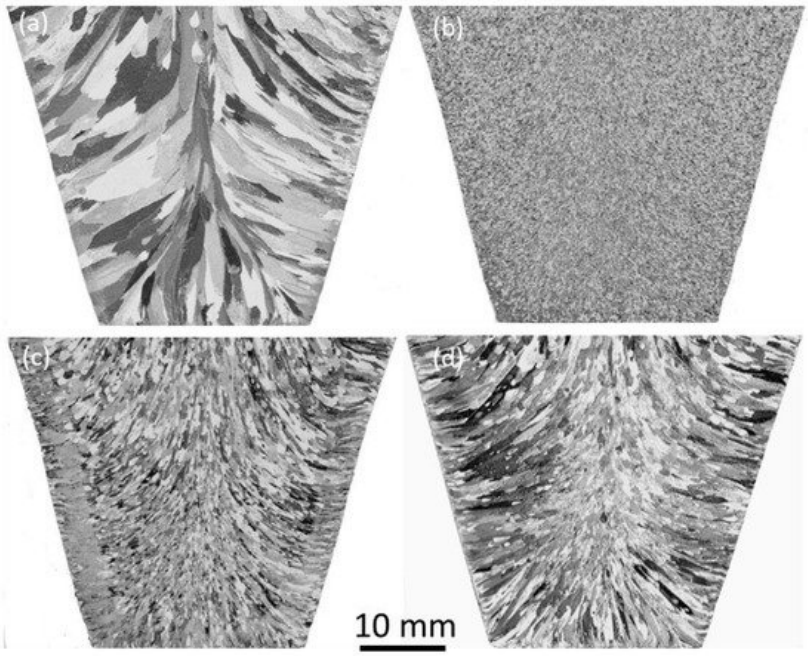

Figure 5. Grain structures of CP-Al solidified in TP-1 mold showing that synthetic TiB_2 particles have no grain refining ability [11]. Macrographs of grain structures at longitudinal sections of CP-Al (**a**) without any addition; (**b**) with addition of 0.2% commercial Al-5Ti-1B grain refiner; (**c**) with addition of synthetic TiB_2 particles; and (**d**) with both synthetic TiB_2 and excess Ti (TiB_2 numbers and excess Ti are equivalent to those of 0.2% Al-5Ti-1B).

2.3. Ti Segregation at Al/TiB_2 Interface

The high resolution STEM HAADF image in **Figure 6**a shows the interface between Al and a TiB_2 particles from the Al-5Ti-1B grain refiner, where the electron beam is along the $[1\ 1\ 2\bar{0}]_{TiB2}$ direction but off from any low-index zone axis of α-Al. An atomic monolayer is clearly seen on the (0 0 0 1) surface of the TiB_2, with the spacing between the atomic monolayer and the surface $(0\ 0\ 0\ 1)_{TiB2}$ plane being measured as 0.25 nm, compared to 0.32 nm of the *d*-spacing of $(0\ 0\ 0\ 1)_{TiB2}$ planes [11]. SuperSTEM/EELS maps in **Figure 6**b–d reveal the chemical nature of the local region across the Al/TiB_2 interface, confirming that the atomic monolayer contains Ti atoms [11]. According to the experimental evidence of structure and chemistry, and supported by results obtained by MD simulation [15], this Ti segregation layer was, therefore, identified as Al_3Ti 2-dimesional compound (2DC) [11]. **Figure 7**a–c show schematically the atomic arrangement of (0 0 0 1)TiB_2, Al_3Ti 2DC layer and (1 1 1) Al plane respectively, and the schematic in **Figure 7**d is the 3-dimensional construction of the monolayer on the (0 0 0 1) surface of TiB_2.

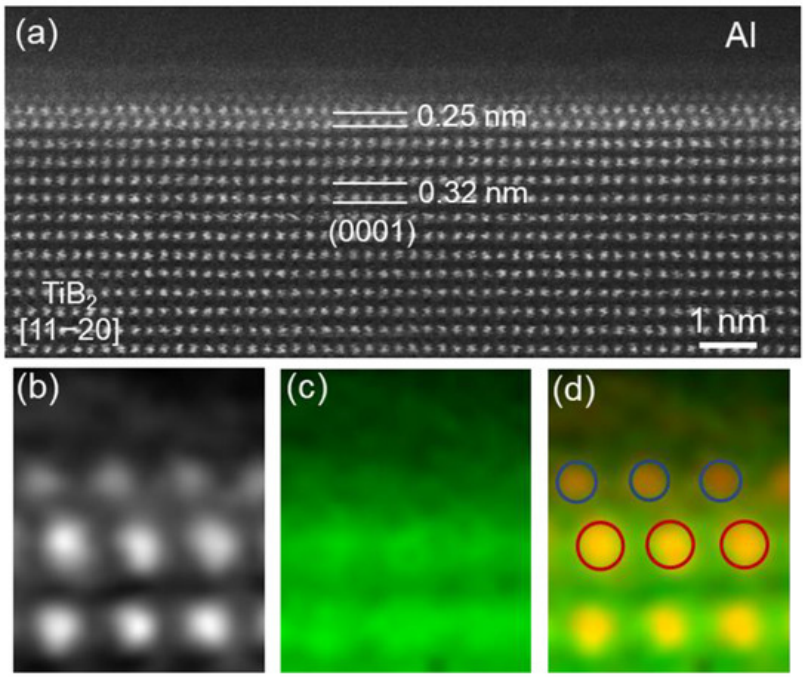

Figure 6. Segregation of Ti at Al/TiB_2 interface [11]. (**a**) Z-contrast STEM-HAADF image; (**b**) local Z-contrast HAADF image across the Al/TiB_2 interface; (**c**) atomic resolution EELS map of Ti K-edge; and (**d**) superimposition of the local image and

Ti K-edge map. The atomic columns with blue circles are Ti atoms-rich columns, and those with red circles are Ti columns of TiB_2. The atomic resolution EELS mapping confirms that the atomic monolayer at the interface contains Ti atoms.

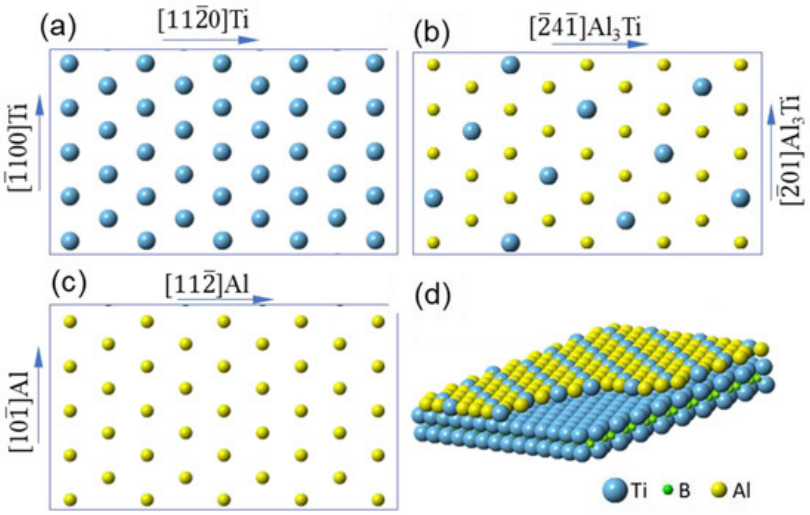

Figure 7. Atomic arrangement of the matching planes at the interface between Al, Al_3Ti 2DC and TiB_2 [11]. Schematics showing (**a**) Ti atoms in (0 0 0 1)TiB_2 plane; (**b**) Ti and Al atoms in (1 1 2)Al_3Ti plane; (**c**) Al atoms in (1 1 1)Al plane; and (**d**) 3D illustration of Al_3Ti 2DC on the TiB_2 surface.

MD simulation was conducted by Qin and Fan to investigate the involvement of Al_3Ti in the heterogeneous nucleation of Al on TiB_2 at an atomistic scale [15]. It was found that a two-dimensional Al_3Ti layer might remain on TiB_2 at a temperature above the Al liquidus. The simulation results showed that this 2D Al_3Ti underwent interface reconstruction by forming a triangular pattern, which consisted of different alternative stacking sequences. The transition region between the triangles forms an area of strain concentration. Through this mechanism, the interfacial Al_3Ti layer stabilizes itself by localizing the large misfit strain between TiB_2 and Al_3Ti.

The heterogeneous nucleation behavior of Al on TiB_2/Al_3Ti substrates was analyzed by Wang et al. [16] using AIMD simulations. Structural ordering was clearly seen in the liquid close to the TiB_2 and Al_3Ti substrates at temperatures below the Al melting point. They found that the Ti-terminated TiB_2 surface had greater potential to nucleate Al. In particular, they observed that, compared to the TiB_2 substrate, the ordering in liquid Al close to the (1 1 2) terminating surface of Al_3Ti substrate was stronger on the Al_3Ti substrate and that the liquid Al readily transformed into a solid fcc-like structure at a smaller undercooling. This verified the higher nucleation potency of Al_3Ti over TiB_2. Simulations by Ma et al. [17] also revealed an almost fully ordered liquid Al layer on (0 0 0 1)TiB_2 substrates.

The nucleation potency of a substrate is usually reflected, to a certain extent, by the lattice misfit at the interface between the substrate and the nucleated new solid phase at the moment of nucleation. According to OR2, the lattice misfit between Al and TiB_2 at the interface is −4.22% at 660 °C, and the misfit decreases to 0.09% when the Al_3Ti 2DC layer is formed. This means that the formation of the Al_3Ti 2DC on the TiB_2 surface results in a significantly increased nucleation potency of TiB_2 particles by the much-reduced absolute lattice misfit.

A bulk Al_3Ti phase is stable in an Al-Ti alloy melt only when Ti concentration is greater than 0.15% according to the Al-Ti equilibrium phase diagram. However, Al_3Ti 2DC could be stable at the metal/substrate interface at a much lower Ti concentration of the bulk melt, driven by reduction of interfacial energy, due to Ti segregation according to Gibbs adsorption theorem, as shown by the theoretical analysis in [18]. This is the case of the present work where Al_3Ti 2DC is readily observed on the (0 0 0 1) surface of TiB_2 particles. Further experiment demonstrated that the Al_3Ti 2DC layer could be deliberately formed on the surface of synthetic TiB_2 particles by interfacial Ti segregation [11]. As shown in **Figure 8**a,b, the synthetic TiB_2 particles treated by melt shearing in Al-Ti alloy melt for 10 min at 850 °C became highly effective in grain refining CP-Al (**Figure 8**b) [11], comparable to those in a commercial Al-5Ti-1B grain refiner (**Figure 5**b). However, the pre-existing Al_3Ti 2DC could be dissolved from the TiB_2 surface. TiB_2 particles from a commercial Al-5Ti-1B grain refiner have been seen to have no grain refining ability after being held in a CP-Al melt at 720 °C for 78 h (**Figure 8**c) or treated in the CP-Al melt by high shear at the temperature for 45 min (**Figure 8**d), respectively [11]. The result verified that Al_3Ti 2DC, instead of TiB_2 itself, is responsible for the increased potency and, thus, the significant refining effectiveness of the commercial Al-5Ti-1B master alloys.

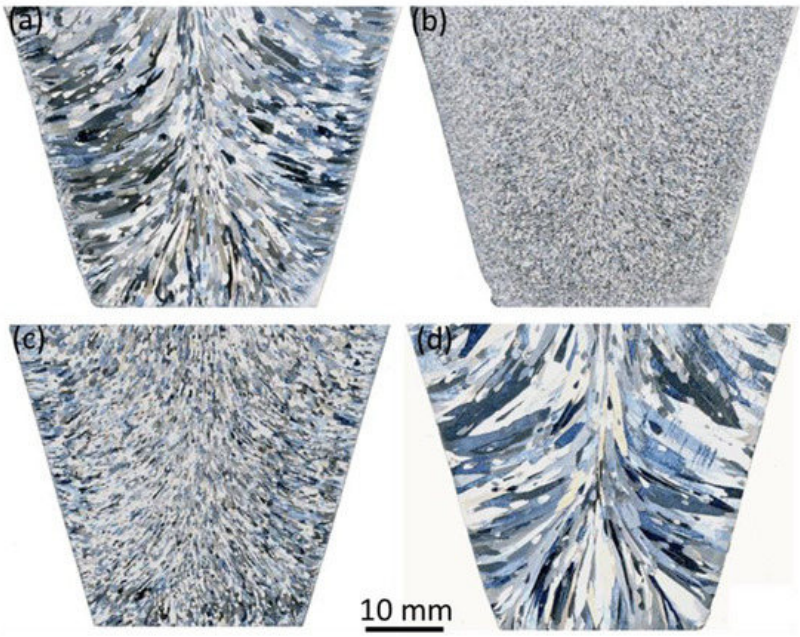

Figure 8. Grain structures of TP-1 cast CP-Al ingots reflecting the formation and dissolution of Al_3Ti 2DC on TiB_2 surface [11]. (**a**,**b**) With the addition of self-made Al-1Ti-0.2B master alloy (the excess Ti and TiB_2 number density are equivalent to those of the addition of 0.2% Al-5Ti-1B grain refiner) from synthetic TiB_2 particles in Al-Ti melt by intensive melt shearing at 850 °C for (**a**) 2 min and (**b**) 10 min, showing grain refinement in (**b**) (indicating the formation of Al_3Ti 2DC on the synthetic TiB_2 after melt shearing for 10 min); and (**c**,**d**) with addition of commercial Al-5Ti-1B grain refiner and then the melt was (**c**) held at 720 °C for 78 h or (**d**) treated by melt shearing for 45 min at 720 °C, showing no grain refinement (indicating dissolution of Al_3Ti 2DC from TiB_2 surface).

The difference between the TiB_2 particles from commercial Al-Ti-B grain refiners and the synthetic ones is that the former have the Al_3Ti 2DC layer on their surface, with the 2DC layer being readily formed at the high processing temperature and high excess Ti concentration during the production processes of the grain refiners.

Grain refinement of Al alloys achieved by addition of Al-5Ti-1B grain refiner is attributed to the factors below:

(i) Formation of Al_3Ti 2DC on the surface of TiB_2 particles during the grain refiner production process, which significantly increased the potency of TiB_2 for nucleation of α-Al;

(ii) Sufficient numbers of added TiB_2 particles which were coated with the Al_3Ti 2DC layer, and suitable particle size and size distribution, which guaranteed sufficient number of grains to be initiated and grown from the nucleating TiB_2 particles and achieved grain refinement;

(iii) Excess Ti in the alloy melt after grain refiner addition generated growth restriction, which increased the effectiveness of the grain refiner by allowing more TiB_2 particles to be active for heterogeneous nucleation, which, in turn, promoted the columnar-to-equiaxed transition.

2.4. Zr Segregation at Al/TiB_2 Interface

Zr-containing Al- alloys are usually difficult to be grain refined by commercial Al-Ti-B grain refiners with standard addition rates [19][20][21][22][23][24][25]. Experiments have demonstrated that addition of Zr, even in a concentration of as low as a few hundred ppm, to Al alloy melts inoculated by Al-Ti-B grain refiner would result in no grain refinement after solidification [2][19][22]. The loss of grain refining ability for Al-Ti-B grain refiners caused by Zr addition is referred to as “Zr poisoning”. The refined grain structure (**Figure 9**a,c) of CP-Al by Al-5Ti-1B grain refiner is replaced by a coarse and columnar one (**Figure 9**b,d) when 0.0558% (558 ppm) Zr is added to the Al melt [26][27].

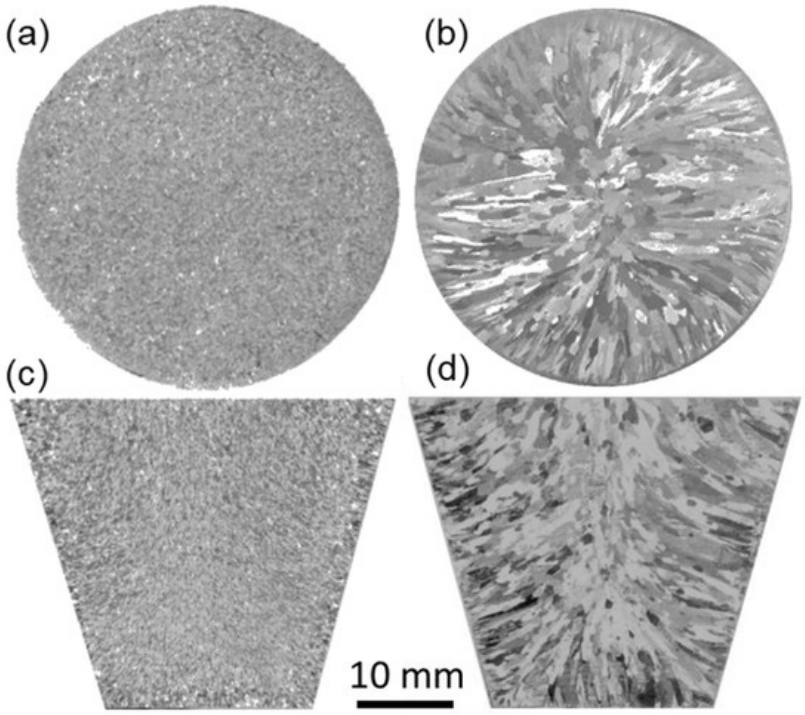

Figure 9. Grain structures of TP-1 cast CP-Al ingots showing Zr poisoning on Al-5Ti-1B grain refiner [26][27]. (**a**,**c**) With addition of 0.2% commercial Al-5Ti-1B grain refiner and (**b**,**d**) with additions of both 0.2% of the grain refiner and 558 ppm Zr, showing that the grain refiner lost its ability to grain refine CP-Al when the small amount of Zr was present in the melt. (**a**,**b**) Transverse and (**c**,**d**) longitudinal sections.

STEM examinations of TiB_2 particles introduced to the Al-Zr alloy melts by addition of a commercial Al-5Ti-1B grain refiner were carried out to study the effect of Zr on TiB_2 particles [26]. STEM HAADF image and the corresponding super-X EDS maps across the Al/TiB_2 interface are shown in **Figure 10**, where Zr enrichment at the interface is clearly seen (**Figure 10**b), even at such a low Zr concentration (558 ppm). The Zr segregation corresponds to the brighter contrast of the interfacial layer seen in the HAADF image (**Figure 10**a). **Figure 10**c,d indicate that the main impurities in the alloy melt, Fe and Si, did not segregate at the interface.

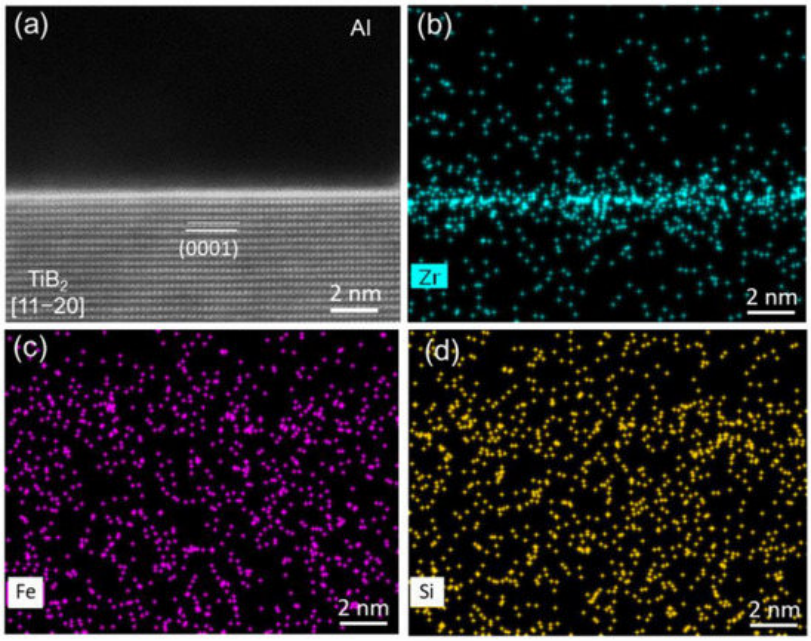

Figure 10. Zr segregation at Al/TiB_2 interface [26]. (**a**) STEM-HAADF image across Al/TiB_2 interface viewed along [1 1 2¯0] TiB_2 direction, and (**b**–**d**) super-X EDS elemental mapping of (**b**) Zr (cyan), (**c**) Fe (purple) and (**d**) Si (yellow) across the interface, showing Zr segregation but no segregation of Fe and Si at the interface.

STEM HAADF imaging at high magnifications reveals that the Zr interfacial segregation results in the formation of an atomic monolayer at the Al/(0 0 0 1)TiB_2 interface, with the atomic columns in the monolayer being brighter than the Ti columns in the (0 0 0 1) plane of TiB_2, as shown in **Figure 11**a, where the interface is viewed along [1 1 2¯0]TiB_2 direction [26]. The higher brightness of the atom columns verifies the presence of heavier Zr atoms (than Ti) in the monolayer. When

viewed along [1 0 1¯0]TiB_2 direction, the brighter atomic columns of the monolayer appear in a periodic pattern, i.e., one bright column between two darker ones, as shown in **Figure 11**b. This suggests that, apart from Zr atoms, there is at least one type of other atom in the layer, with the in-plane atomic arrangement being ordered.

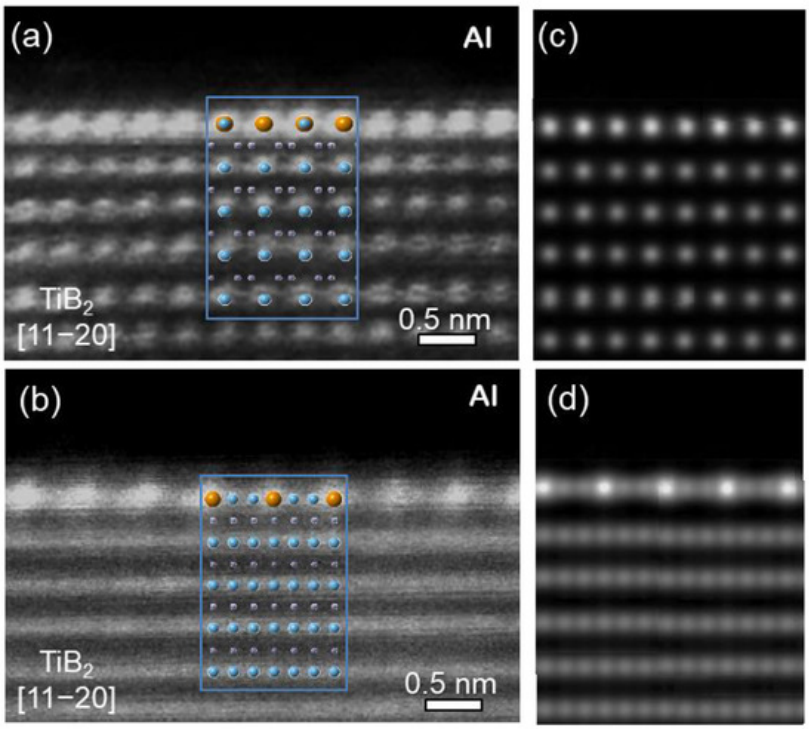

Figure 11. Formation of Zr segregation layer (Ti_2Zr 2DC) at Al/TiB_2 interface [26][27]. (**a**,**b**) STEM-HAADF images compared with (**c**,**d**) simulated ones in [1 1 2¯0] TiB_2 and [1 0 1¯0]TiB_2 direction, respectively. The simulation STEM HAADF images was carried out using the QSTEM multi-slice simulation package developed by Koch [28] according to the constructed super-lattice structure of Ti_2Zr 2DC based the experimental HR-STEM observation.

According to the experimental evidence of both structure and chemistry, the interfacial segregation layer is identified as Ti_2Zr 2DC [26][29], with its in-plane atomic arrangement and 3D construction being shown schematically in **Figure 12**a,b, respectively. With the inputs derived from the atomic configuration of the Ti_2Zr 2DC, HAADF image simulation was carried out using the QSTEM multi-slice package [28]. The simulation result in **Figure 11**c,d is in good agreement with the experimental images in **Figure 11**a,b along both [1 1 2¯0]TiB_2 and [1 0 1¯0]TiB_2 directions, validating the nature of the Zr segregation layer at the interface. Formation of the Ti_2Zr 2DC layer resulted from the substitution of one third of Ti atoms in the top (0 0 0 1) Ti plane of TiB_2 by Zr atoms from the melt, which was possibly due to ZrB_2 being thermodynamically more stable than TiB_2. However, further penetration of Zr atoms into the TiB_2 crystal structure beyond the top (0 0 0 1) Ti plane is difficult due to the presence of the layer of B atoms beneath the Ti_2Zr 2DC, which have strong covalent bonds between the B atoms. Formation of any bulk ZrB_2 or $(Zr_xTi_{1-x})B_2$ are kinetically unfavorable, even if they are thermodynamically feasible, as suggested in the literature [19][30][31].

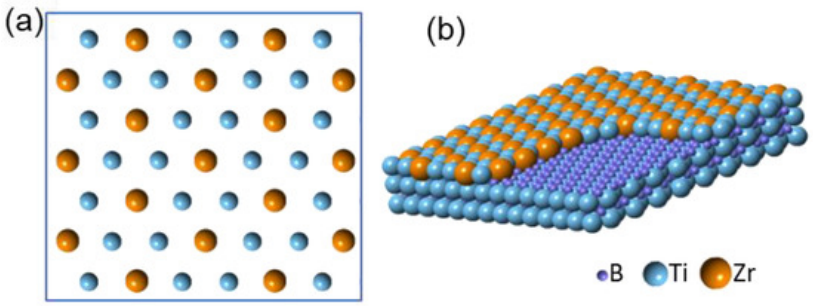

Figure 12. Crystal structure and chemistry of the Zr segregation monolayer (Ti_2Zr 2DC) at Al/TiB_2 interface [26]. (**a**) In-plane arrangement of Zr (larger orange spheres) and Ti (smaller blue spheres) atoms in the Ti_2Zr 2DC layer and (**b**) 3D construction of the Ti_2Zr 2DC on (0 0 0 1)TiB_2 surface.

Atomic ordering in the liquid Al adjacent to the TiB_2 substrate at a temperature close to the alloy liquidus has been carried out by ab initio MD simulations (AIDM) for the Al(*l*)/TiB_2 (Ti_2Zr 2DC) system at 900 K, 1000 K and 1200 K, respectively [26]. **Figure 13**a shows the snapshot of the system equilibrated at 1000 K viewed along the [1 0 1¯

0]$_{TiB2}$ direction, and **Figure 13**b shows the atomic density profiles of the liquid Al adjacent to the Al(*l*)/TiB_2 (Ti_2Zr 2DC) interface equilibrated at the three different temperatures. It is clear from the experimental evidence in **Figure 11** that the Zr atoms present in the Ti_2Zr 2DC layer protrude into the liquid Al. This protrusion of Zr atoms is evident in the atomic density profile in **Figure 13**b where the peak for Ti_2Zr 2DC is seen to be separated into two sub-peaks, marked as Ti and Zr. Quantified by the atomic density profile, the central positions of the Zr atoms in the 2DC layer were 0.45 Å away from that of the Ti atoms, which represents 19% of Al (1 1 1) *d*-spacing (0.2338 nm). This meant that the formation of Ti_2Zr 2DC on the (0 0 0 1) TiB_2 surface introduced a 19% atomic roughness to the TiB_2 surface. The consequent effect of the 2DC formation was that the atomic ordering in the liquid Al adjacent to the L/S interface was significantly weakened; only two clear peaks are shown in the atomic density profile (**Figure 13**b), compared with 6 peaks on an atomically flat substrate surface [32]. In addition, the protrusion of Zr atoms in the Ti_2Zr 2DC existed over a wide range of temperatures of 900 to 1200 K.

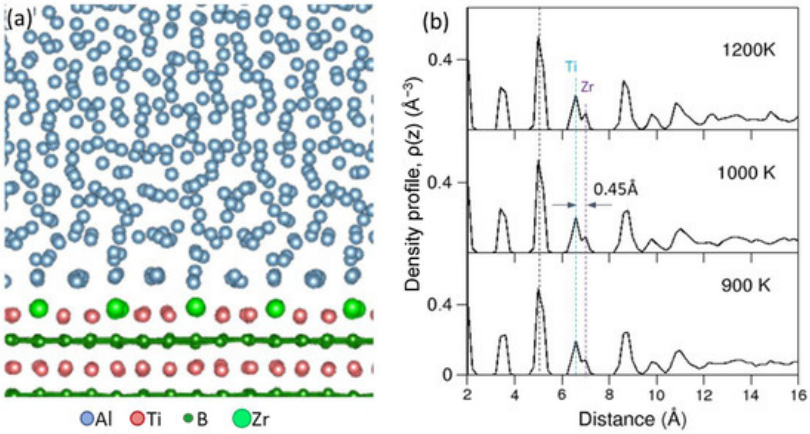

Figure 13. Ab initio MD simulation of Zr segregation at Al/TiB_2 interface [26]. (**a**) Snapshot of Al(liquid)/TiB_2(Ti_2Zr 2DC) interface along [1 0 1¯0] TiB_2 (Ti_2Zr 2DC) direction simulated at 1000 K and (**b**) atomic density profiles ρ(z) across the Al(liquid)/TiB_2 (Ti_2Zr 2DC) interface simulated at 900 K, 1000 K and 1200 K, respectively. The dotted lines in (**b**) indicate the position of the Ti and Zr atoms in the Ti_2Zr 2DC.

With Zr being in Al alloy melts, the pre-existing Al_3Ti 2DC on the TiB_2 surface becam thermodynamically unstable and dissolved. Due to the higher thermodynamic stability of ZrB_2 than that of TiB_2 [19][30], Zr atoms from the melt gradually substituted for some of the Ti atoms in the top (0 0 0 1) TiB_2 plane and the Ti_2Zr 2DC structure was, thus, formed. **Figure 14** shows the on-going process of the Ti_2Zr 2DC formation on the TiB_2 surface, where the 2DC layer seen at the left-hand side would extend to cover the whole (0 0 0 1) surface of the TiB_2 particle with proceeding of the segregation process [26].

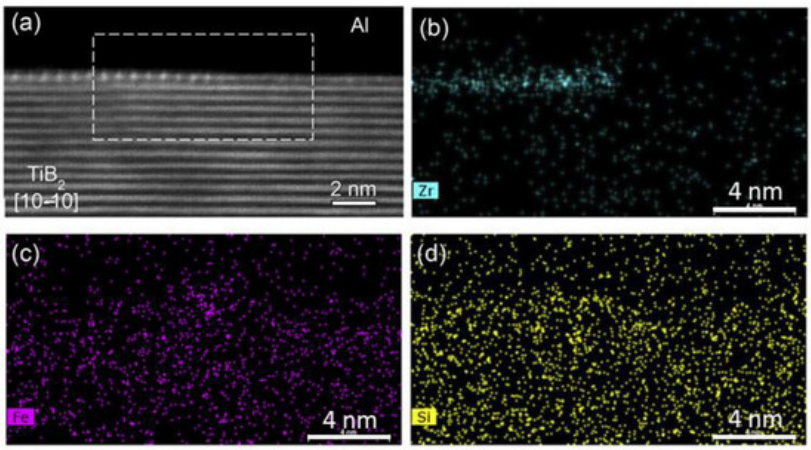

Figure 14. On-going of the Zr segregation process [26]. (**a**) STEM HAADF image across Al/TiB_2 interface viewed along [1 0 1¯0] TiB_2 direction, and (**b**–**d**) super-X EDS elemental mapping of (**b**) Zr, (**c**) Fe and (**d**) Si, showing the formation of Zr_2Ti 2DC layer on the left-hand side, but not yet on the right-hand side of the (0 0 0 1) TiB_2 surface.

The Ti_2Zr 2DC layer was coherent with (0 0 0 1) TiB_2 plane, so the lattice misfit between the 2DC layer and Al was back to the value of −4.22%. The small lattice misfit 0.09% between Al_3Ti 2DC and Al no longer existed. This would make the TiB_2 particles with Ti_2Zr 2DC impotent for heterogeneous nucleation of α-Al.

The spacing between Ti_2Zr 2DC layer and the first (0 0 0 1) Ti plane was experimentally measured as 0.34 nm, larger than 0.32 nm of d-spacing of (0 0 0 1)Ti planes. As shown above, ab initio MD simulations performed for the Al(liquid)/TiB_2

(Ti_2Zr 2DC) system revealed that the Zr atoms in Ti_2Zr 2DC protruded into the liquid Al by 0.45 Å [26]. This meant that formation of Ti_2Zr 2DC resulted in roughness at the atomic level on the TiB_2 surface. The simulation also demonstrated that, with such a large lattice misfit and atomically rough surface, the atomic ordering in the liquid Al adjacent to the Al(*l*)/TiB_2 interface was significantly weakened [26], indicating a great decrease in nucleation potency of the TiB_2 particles with Ti_2Zr 2DC.

The mechanism underlying "Zr poisoning" of Al-Ti-B grain refiners is closely related to the dissolution of the pre-existing Al_3Ti 2DC on the TiB_2 surface in the commercial Al-Ti-B based grain refiners and the formation of Ti_2Zr 2DC in Al-Zr melt, rendering the TiB_2 particles impotent for heterogeneous nucleation of α-Al. With addition of Zr to Al alloy melts, despite a concentration as low as a few hundred ppm, the Zr atoms tend to segregate at the TiB_2/melt interface, resulting in the following effects: (i) dissolution of the pre-existed Al_3Ti 2DC on the TiB_2 surface; (ii) the segregated Zr atoms at the interface substituting for some of the Ti atoms in the (0 0 0 1) surface to form the Ti_2Zr 2DC atomic layer; and (iii) the Ti_2Zr 2DC layer becoming atomically rough due to the considerably larger atomic size of Zr than that of Ti. The increased amplitude of lattice misfit (from 0.09% to 4.22%) and atomically roughened particle surface render TiB particles impotent for heterogeneous nucleation and they are, thus, poisoned.

2.5. Si Segregation at Al/TiB_2 Interface

Si is also one of those elements which give rise to a poisoning effect on Al-Ti-B grain refiners. Experiments have shown that the Al-Ti-B based grain refiners are not effective for grain refining Al-Si alloys containing high Si concentrations [33]. As shown in **Figure 15**, the grain structure of Al-2.0Si alloy is refined by inoculation of 0.2% Al-5Ti-1B grain refiner with the average grain size being 195 ± 22 µm. However, the Al-8.4Si alloy added with the same amount of the grain refiner shows a much coarser microstructure, with the average grain size being 686 ± 73 µm, although the grain structure remains equiaxed. The experimental results in previous studies agree that, when inoculated with Al-Ti-B grain refiners with usual addition rates (0.1~0.2%), the grain size of hypoeutectic Al-Si alloys decreases marginally with increasing Si concentration until about 2–3% and then it starts increasing with further increase in Si content, as shown by the representative data collected from the literature in **Figure 16**, plotted in Ref. [33].

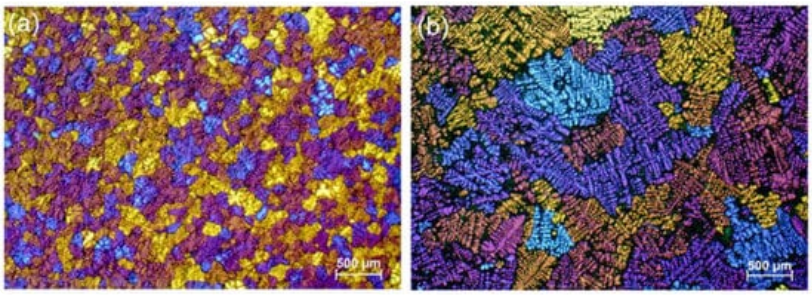

Figure 15. Si poisoning on Al-5Ti-1B grain refiner when its concentration is >3.0% [33]. Optical micrographs showing microstructure of 0.2% Al-5Ti-1B inoculated (**a**) Al-2Si and (**b**) Al-8.4Si alloy solidified in TP-1 mold, showing the much coarser grain size of Al-8.4Si than that of Al-2Si.

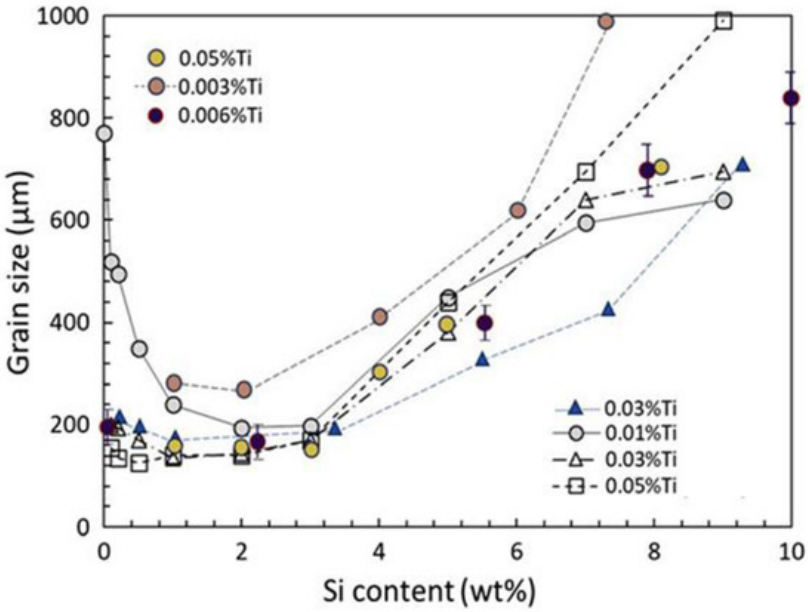

Figure 16. Grain size of binary Al-Si alloys (inoculated by Al-Ti-B grain refiner) as a function of Si concentration (the data were collected from the literature and plotted in Ref. [33]). The representative data collected from the literature showing the variation of the grain size with Si content of binary Al-Si alloys inoculated with Al-5Ti-1B grain refiner.

STEM/super-X EDS analysis on chemical profiles of the local region across the Al/TiB_2 interface reveals Si segregation at the interface [33]. As shown in **Figure 17**, a peak at the position of energy 1.74 keV, i.e., the characteristic Kα peak of Si, is clearly seen in the EDS spectrum in **Figure 17**b, which was acquired from the Al/TiB_2 interfacial region, and the Si interfacial segregation is also shown in the corresponding EDS Si map in **Figure 17**c. Fe, as one of the main impurities in CP-Al, was not detected at the interface (**Figure 17**d). EDS analysis indicated that Si segregation at Al/TiB_2 interface was common to all the tested TiB_2 particles collected from Al-Si alloys containing 2–10% Si and 0.2% Al-5Ti-1B grain refiner [33].

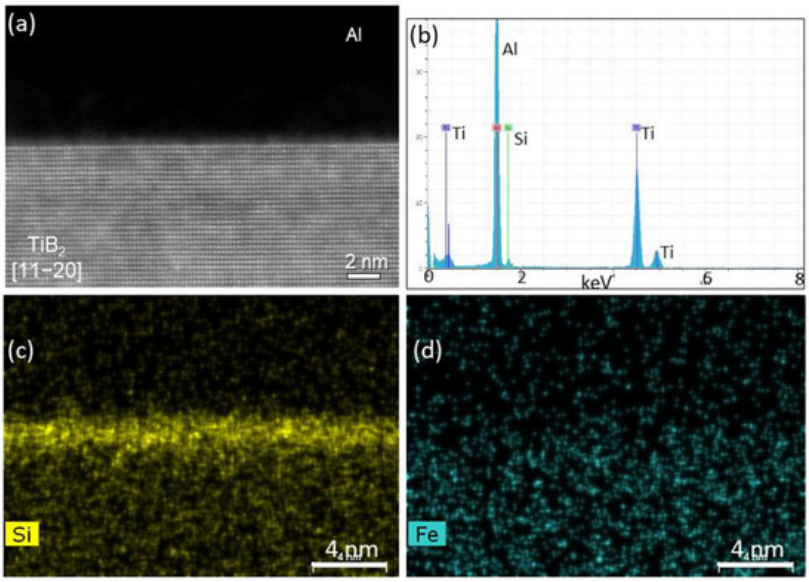

Figure 17. Si segregation at Al/TiB_2 interface data from [33]. (**a**) STEM-HAADF image of Al/TiB_2 interface for a TiB_2 particle from Al-8.4Si alloy containing 0.2% Al-5Ti-1B grain refiner; (**b**) Super-X EDS spectrum acquired from the interface; and (**c**,**d**) super-X EDS mapping of (**c**) Si and (**d**) Fe.

As shown earlier, TiB_2 particles in commercial Al-Ti-B grain refiners are covered by an Al_3Ti 2DC layer on their surfaces due to Ti segregation and the 2DC layer is responsible for the powerful ability for grain refinement. However, high resolution STEM examinations of multiple TiB_2 particles which had been added to Al-Si alloy melts, revealed that the pre-existing Al_3Ti 2DC on TiB_2 surface was missing. **Figure 18** shows the Al/TiB_2 interface viewed from [1 1 2¯

0]TiB_2 direction of a TiB_2 particle from Al-8.4Si alloy melt, where no extra atomic layer, other than the (0 0 0 1)Ti layer of TiB_2, is seen, indicating the disappearance of the Al_3Ti 2DC [33].

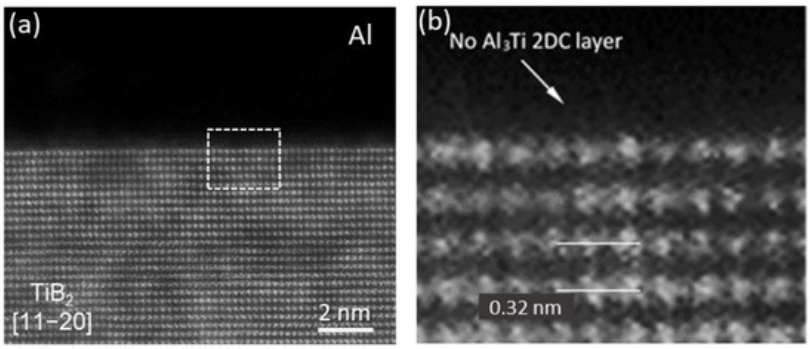

Figure 18. Disappearance of Al_3Ti 2DC at Al/TiB_2 interface in Al-Si melt [33]. High resolution STEM-HAADF images of (**a**) Al/TiB_2 interface and (**b**) zoom of the marked local region across the interface viewed along [1 1 2¯0] TiB_2 direction for a TiB_2 particle (by addition of Al-5Ti-1B grain refiner) in Al-8.4Si alloy melt, showing that the pre-existing Al_3Ti 2DC layer on the (0 0 0 1)TiB_2 surface is no longer there.

It is believed that, when TiB_2 particles are added to Al-Si melt, the Al_3Ti 2DC on their surface is not stable and dissolves into the melt. Evidence of such dissolution was experimentally observed in Al-Si alloys with a low Si concentration. **Figure 19** shows the on-going dissolution of Al_3Ti 2DC where the 2DC layer remained on the left-hand side but was missing on

the right-hand side of the (0 0 0 1) TiB_2 surface. The remainder of the 2DC layer was more readily observed in low Si Al-Si alloys than in high Si ones, indicating that Al_3Ti 2DC was more unstable thermodynamically and kinetically, and, thus, dissolved faster in a high Si Al-Si melt than in a lower Si Al-Si melt [33].

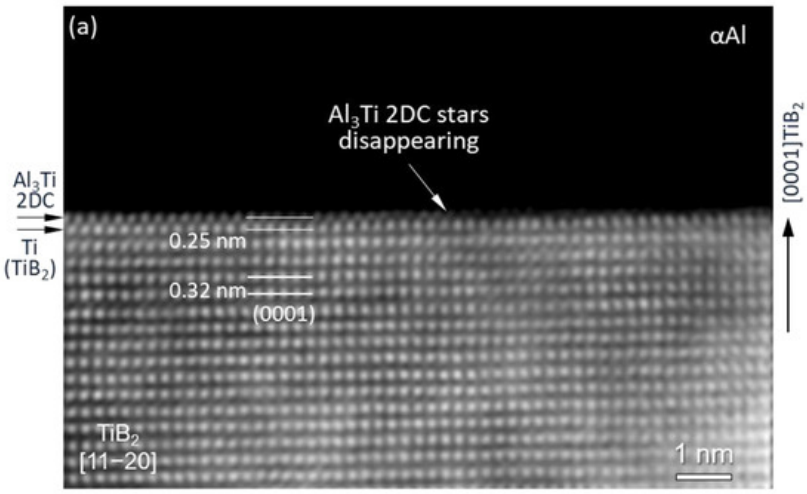

Figure 19. On-going of the dissolution process of Al_3Ti 2DC at Al/TiB_2 interface [33]. High resolution STEM HAADF image of the Al/TiB_2 interface viewed along [1 1 2¯0] TiB_2 direction, showing the remaining Al_3Ti 2DC layer on the left-hand side of the (0 0 0 1) surface of TiB_2 particle added to Al-2Si alloy melt.

Si segregation does not lead to the formation of any 2DC layer or 3D bulk phase at the Al/TiB_2 interface. According to the Gibbs adsorption isotherm, solute segregation driven by interfacial energy reduction occurs only in one or two atomic layers. It is believed that Si enrichment by segregation at the interface can be considered a 2-dimensional solution (2DS), different from the cases of segregation of Ti or Zr, where in-plane ordered Al_3Ti 2DC [11] or Ti_2Zr 2DC [26] resulted at the Al/TiB_2 interface, respectively.

Dissolution of Al_3Ti 2DC due to Si segregation results in the reduced nucleation potency of TiB_2. As shown earlier, nucleation of α-Al now takes place directly on the (0 0 0 1) surface of TiB_2 with a much increased lattice misfit −4.22% between {0 0 0 1}TiB_2 and {1 1 1}Al instead of the small value 0.09% between Al_3Ti 2DC and {1 1 1}Al at the interface. The mechanism for Si poisoning is, therefore, identified as.

- Si interfacial segregation leads to enrichment of Si at the Al-Si melt/TiB_2 interface. The higher the Si concentration in the melt, the more Si enrichment at the interface there is.
- Si segregation at the Al-Si/TiB_2 melt interface makes the pre-existed Al_3Ti 2DC layer unstable on the TiB_2 surface, and, thus, the 2DC dissolves gradually, resulting in a greatly decreased nucleation potency for the TiB_2 particles. The dissolution rate of the 2DC layer increases with increasing Si enrichment at the interface.
- The subsequence of the 2DC dissolution is a reduced total number of potent TiB_2 particles available for heterogeneous nucleation and grain initiation of α-Al, and, hence, an increased grain size.

2.6. Fe Segregation at Al/TiB_2 Interface

Fe segregation has not been observed at the Al/TiB_2 interface when its concentration is in an impurity level, e.g., ~0.08% in a commercial purity (99.8%) Al [26][33]. However, Fe readily segregates at the interface when a relatively high Fe concentration, e.g., a few percent, is present in Al melt [34][35][36][37]. **Figure 20** shows Fe segregation at Al/$(1\ 1\ 0\ 0)_{TiB2\ (AlB2)}$ interface in a sample in which the boride particles were in-situ synthesized by reaction of Al-8Fe and Al-10Ti master alloys in the CP-Al melt at 920 °C. **Figure 20**a shows that a Fe-rich interfacial segregation layer on the prismatic surface of TiB_2 formed in a zig-zag fashion when viewed along [1 1 2¯

$0]_{TiB2}$ direction, with its atomic arrangement being schematically illustrated in **Figure 20**b. The EDS mapping in **Figure 20**d across the interface region in **Figure 20**c confirmed the Fe segregation at the interface. Interestingly, no Fe segregation was on the {0 0 0 1} basal surface of TiB_2.

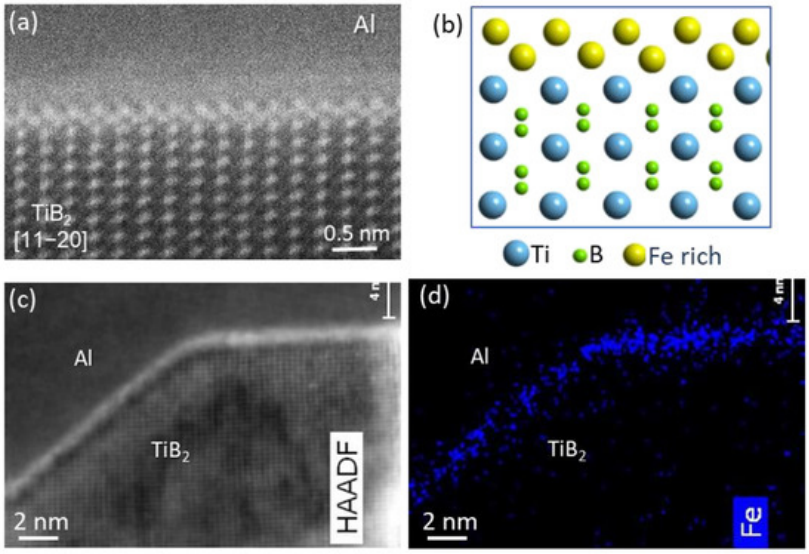

Figure 20. Fe segregation at the Al/(1 1 0 0)TiB_2 (AlB_2) interface [34][35][36]. (**a**) High resolution STEM HAADF image showing the extra atomic layers at the interface when viewed from [1 1 2¯0]TiB_2 direction; (**b**) schematic showing the zig-zag atomic arrangement of the interfacial layers viewed along the direction; and (**c**) STEM HAADF image and (**d**) superX-EDS mapping confirming the enrichment of Fe at the interface.

The behavior of Fe segregating selectively only on prismatic TiB_2 surfaces has been repeatedly observed, as shown in **Figure 21**, with Fe segregation occurring discontinuously on the prismatic surface, but Si segregation covering both basal and prismatic surfaces of TiB_2. Interestingly, accompanied by Si segregation, there are two atomic layers in the regions where Fe is enriched when observed in $[1\ 1\ 2\bar{0}]_{TiB2}$ direction.

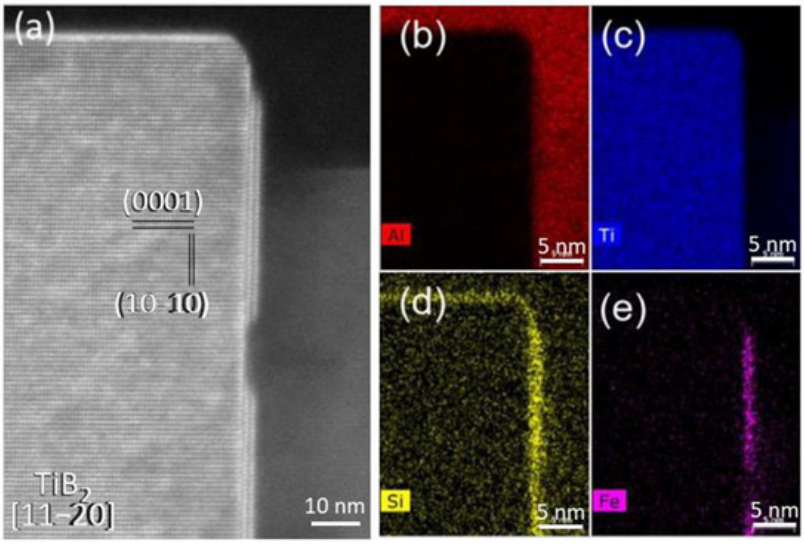

Figure 21. Segregation of Fe and Si at Al/TiB_2 interface [34][38]. (**a**) High resolution STEM HAADF image across Al/TiB_2 interface viewed along [1 1 2¯0] TiB_2 direction; (**b**–**e**) super-X EDS elemental mapping of (**b**) Al, (**c**) Ti, (**d**) Si, and (**e**) Fe showing that Si segregates on all surface of TiB_2 but Fe segregates only on (1 0 1¯0) prismatic surface of TiB_2.

It has been demonstrated that TiB_2 particles with Fe and Si segregation are effective to refine the primary α-$Al_{15}(Fe,Mn)_3Si_2$ intermetallic phase in Al-Fe-Si-Mn alloys, with the size of the intermetallic phase being reduced from a few tens of micrometers to a few of micrometers [34][35][36][37][38]. The Fe- and Si-coated TiB_2 particles are frequently found inside the primary α-$Al_{15}(Fe,Mn)_3Si_2$ phase particles and have specific orientation relationships with the intermetallic phase, suggesting that more of such TiB_2 particles participated in nucleation of the Fe-rich intermetallic compounds [35][36][37][38]. This is because, in addition to a structural templating, an extra compositional templating is provided by segregation of Fe and Si, and, thus, the heterogeneous nucleation and grain initiation processes are enhanced for the intermetallic compounds [34][38].

2.7. Cu Segregation at Al/TiB_2 Interface

Cu is readily observed to segregate at the Al/TiB_2 interface. The STEM HAADE images in **Figure 22** show the interface between Al and both the (0 0 0 1) basal and (1 1 0 0) prismatic surfaces of a TiB_2 particle from an Al-3Ti-1B-4.2Cu alloy. A

brighter layer is visible at the (0 0 0 1)TiB_2 surface, indicating the segregation of the heaver (than Ti) Cu atoms on the (0 0 0 1) basal surface of TiB_2. As shown in **Figure 22**a, Cu seems not to segregate on the prismatic surface of TiB_2.

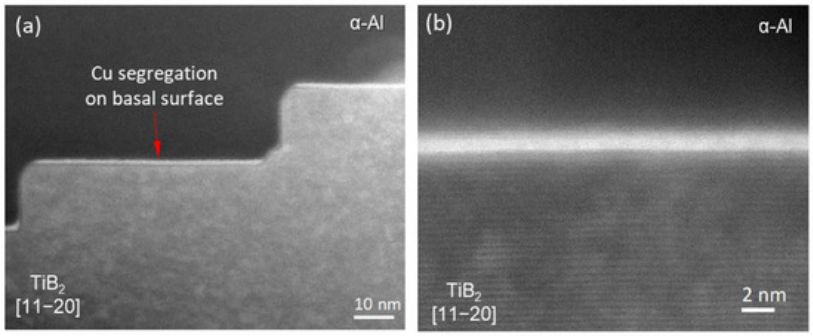

Figure 22. Cu segregation at Al/TiB_2 interface. STEM HADDF images show (**a**) general view and (**b**) local region across the Al/TiB_2 interface for a TiB_2 particle in Al-3Ti-1B-4.2Cu alloy, where a bright segregation layer is visible on the (0 0 0 1)TiB_2 basal surface but not on the (1 1 0 0) prismatic surface of the TiB_2.

In an Al-3.5Cu alloy containing TiB_2 particles which had been introduced by addition of commercial Al-5Ti-1B master alloy, Li et al. [39] observed that there was a Cu-rich layer about 2 nm thick covering both the basal and prismatic plane surfaces of TiB_2 particles. It was further revealed that, on top of the (0 0 0 1) basal plane surface of TiB_2, there was an Al and Ti rich region which was an Al_3Ti 2DC layer, followed by an Al-rich layer with a much lower Ti content, and, finally, a Cu-rich layer of about several atomic planes (2–3 atoms) thick which exhibited in-plane ordering. On the {1 1 0 0} prismatic surface of TiB_2, Cu segregation was also detected, although no Al_3Ti 2DC layer was observed. The observation of an Al_3Ti 2DC layer on the TiB_2 surface was in agreement with the earlier work, with the 2DC layer being formed during the production of the commercial Al-5Ti-1B grain refiner.

It has been seen that segregation of Zr or Si results in dissolution of the pre-existed Al_3Ti 2DC layer. However, Cu segregation apparently does not interfere with the pre-existing Al_3Ti 2DC layer at the Al/TiB_2 interface. Instead, the Cu-rich layer resulting from interfacial segregation was on the top of the Al_3Ti 2DC [39]. Consequently, such a Cu-rich layer at the interface is expected to affect heterogeneous nucleation, although the actual effect has yet to be determined.

3. Segregation at Mg/MgO Interface

3.1. Nature of Native MgO Particles in Mg Alloy Melt

Magnesium oxide (MgO) is readily formed in-situ during heating and melting of Mg alloys due to the very high affinity of Mg with oxygen. The native MgO in Mg alloy melts are usually in the form of films that consist of numerous nano-sized MgO particles [40][41][42][43][44]. The oxide films in Mg alloy melts can be dispersed by means of intensive physical stirring; high shear, for instance, resulting in more discrete particles. **Figure 23** gives such an example where the high shear imposed to the melt is demonstrated to disperse the oxide films in Mg-9Al alloy (**Figure 23**a) and commercial purity Mg (**Figure 23**b) and makes the MgO particles uniformly distribute in the melt (**Figure 23**c,d) [41][42][43][44]. The individual MgO particles are faceted with either {1 1 1} or {1 0 0} planes, being the terminating surfaces, displaying two distinctive morphologies, i.e., {1 1 1} terminated octahedral (**Figure 24**a) and {1 0 0} terminated cubic (**Figure 24**b). The size of the MgO particles follows the log-normal distribution, with the average size being about 70–80 nm [43][44].

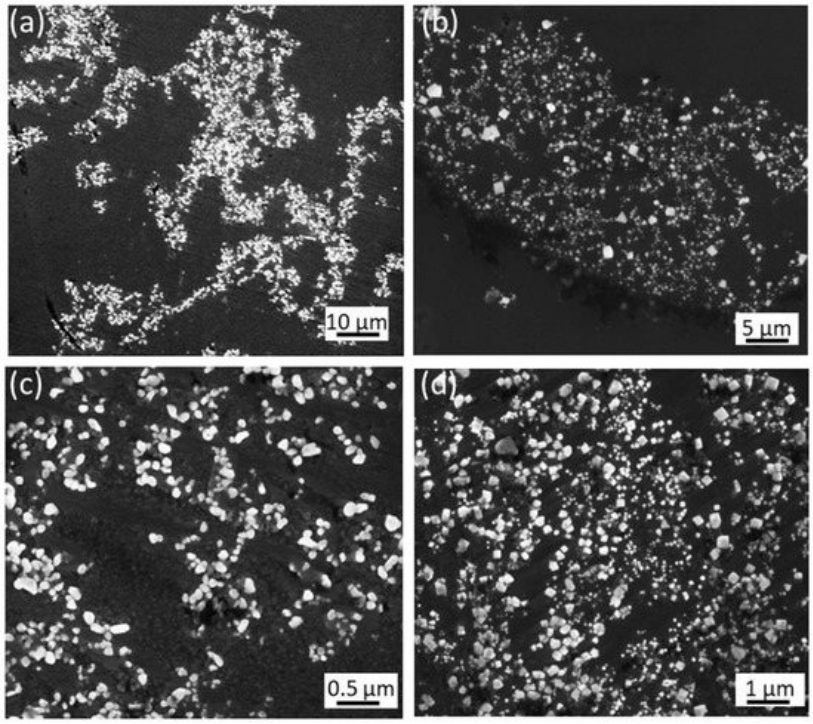

Figure 23. Morphology of MgO films and MgO particles [43]. SEM images showing general morphology of (**a**,**b**) native MgO films and (**c**,**d**) native MgO particles dispersed by melt shearing collected from (**a**,**c**) Mg-9Al and (**b**,**d**) commercial purity Mg melt. The oxide films are liquid films that contain numerous discrete MgO particles.

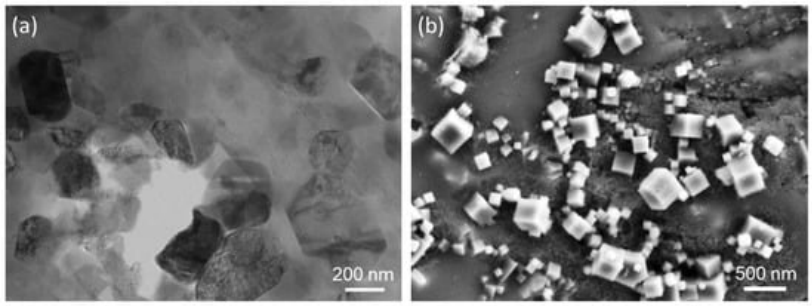

Figure 24. Faceted behaviour of the native MgO particles in Mg alloy melt [41][43][44]. TEM and SEM images showing (**a**) {1 1 1} faceted octahedral and (**b**) {1 0 0} faceted cubic MgO particles in Mg-9Al-1Zn (AZ91) alloy.

3.2. MgO Acting as Nucleation Substrate

Native MgO has been demonstrated to act as an efficient substrate for nucleation of Mg, leading to significant grain refinement and improved mechanical properties for various Mg alloys [41][42][44][45][46][47][48][49][50][51][52][53]. The experimental and theoretical investigations have shown that the key factors for native MgO to achieve grain refinement are its relatively poor nucleation potency and availability of high number density in the melt. The low nucleation potency of MgO enables a large nucleation undercooling ΔT_n which is required for triggering a so-called explosive grain initiation (EGI) scheme [47][53] and the latter ensures numerous solid grains initiate and grow. MgO has a poor lattice matching with Mg at the interface with the lattice misfit of 7.9% when it nucleates Mg solid on its faceted {1 1 1} or {1 0 0} surfaces [40][43]. With intensive melt shearing prior to solidification, the native MgO particles in the melt are well dispersed and the number density of the particles can be as high as ~$10^{17}/m^3$ [54], 3 order of magnitude higher than ~$10^{14}/m^3$ of TiB_2 when 0.1% Al-5Ti-1B grain refiner is introduced in Al melt [14]. Given the current situation in the Mg industry where no commercial grain refiner is available, except Zr, which is only for Al-free Mg alloys, harnessing the native oxides in Mg alloy melts to achieve grain refinement is of great significance [47][53].

3.3. Mg/MgO Interface

Among the two types of morphology, i.e., {1 1 1}MgO and {1 0 0}MgO faceted, the {1 1 1}MgO particles are dominant in terms of particle numbers [41][43]. Well-defined ORs has been observed experimentally by high resolution TEM examinations of multiple MgO particles. As shown in **Figure 25**, two ORs between the two types, MgO and Mg, have been identified as [41][43][44]:

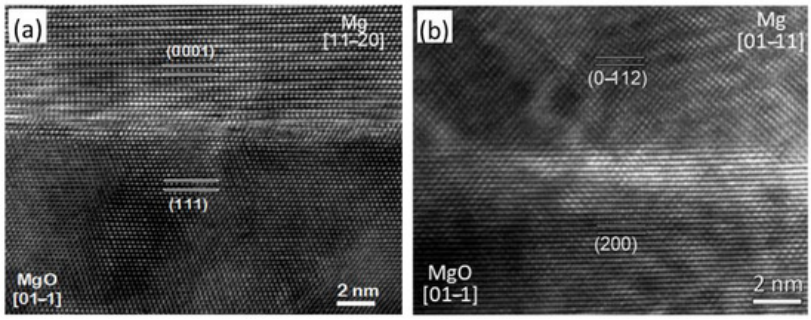

Figure 25. Evidence of heterogeneous nucleation of Mg on MgO particle substrate [41][44]. HR-TEM images viewed in (**a**) [1 1 2¯0]Mg // [0 1 1¯]MgO, and (**b**) [0 1 1¯ 1]Mg // [0 1 1¯]MgO direction, respectively, showing the well defined orientation relationships (ORs) between (**a**) Mg and {1 1 1}Mg, and (**b**) Mg and {1 0 0}MgO.

$$\mathrm{OR\,3:}\ (1\,1\,1)\,[0\,\bar{1}\,1]\,\mathrm{MgO}\ //\ (0\,0\,0\,1)\,[1\,1\,\bar{2}\,0]\,\mathrm{Mg},$$

This is the direct evidence that solid Mg does nucleate heterogeneously on both {1 1 1} and {1 0 0} MgO particles.

Ab initio molecular dynamics (AIMD) simulation has been carried out to study the terminating surfaces of MgO and the ordering of atoms in the local region of melt adjacent to the L-Mg/MgO interface at a temperature above the liquidus, i.e., prenucleation [55]. **Figure 26**a,b shows the snapshots of in-plane view of the newly formed terminating Mg layer on the {1 1 1}MgO surface and the corresponding sideview of the Mg/{1 1 1}MgO interface, respectively, after the thermodynamically equilibrium state was reached during the simulation at 1000 K. The new terminating layer was found to contain vacancies (marked by the crosses in **Figure 26**b), introducing roughness on the atomic scale to the {1 1 1} MgO surface and, thus, greatly weakening the atomic layering in the melt adjacent to the L/S interface, as shown in **Figure 26**b.

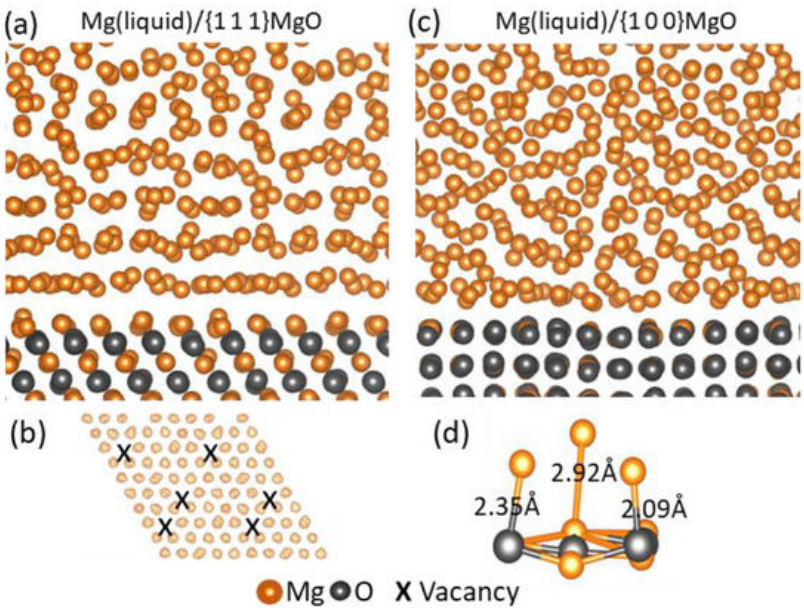

Figure 26. Ab initio molecular dynamics (AIMD) simulation of Mg/MgO interface [55]. (**a**) Mg(l)/MgO{1 1 1} and (**c**) Mg(l)/MgO{0 0 1} interfaces showing atomically rough; (**b**) the first liquid Mg layer induced by the usually O-terminated MgO{1 1 1} substrate, containing vacancies as marked by the "x"; and (**d**) the first liquid Mg layer induced by the MgO{0 0 1} substrate, showing atomically rough due to the varying bond lengths between liquid Mg atoms and the O and Mg ions on the MgO{0 0 1} surface.

Figure 26c,d shows chemical bonding of liquid Mg atoms to the adjacent O and Mg ions in the {0 0 1}MgO substrate and the snapshot of the side view of the Mg/(1 0 0)MgO interface at the equilibrium state in the simulation. The bond length between Mg^{2+} ion on the {1 0 0}MgO surface and Mg atom in the melt was 2.92 Å, 0.8 Å longer than that between O^{2-} ion and Mg atom in the melt (**Figure 26**d), and the surface of {1 0 0} MgO was atomically rough [55]. Consequently, the ability of (1 0 0) MgO to template ordering of the atoms in the melt was strongly reduced, i.e., a decreased prenucleation [55].

3.4. Y Segregation at Mg/MgO{1 1 1} Interface

Yttrium (Y) is one of the rare earth elements which enables high performance of some advanced Mg- alloys, such as the WE series alloys. Y present in Mg alloy melts has been readily found to segregate at the Mg/MgO interface. **Figure 27** shows the experimental evidence of Y segregation in Mg-0.5Y melt at the interface between {1 1 1} faceted MgO and Mg,

where the peaks of yttrium L edge losses clearly appear in the STEM/EELS spectrum in **Figure 26**a (curve 2 in orange), acquired from the local area at Mg/MgO interface. The local STEM HAADF image (**Figure 27**b) from [0 1 1]MgO direction and corresponding EELS elemental map of yttrium (**Figure 27**c) verify the Y segregation at the interface [40].

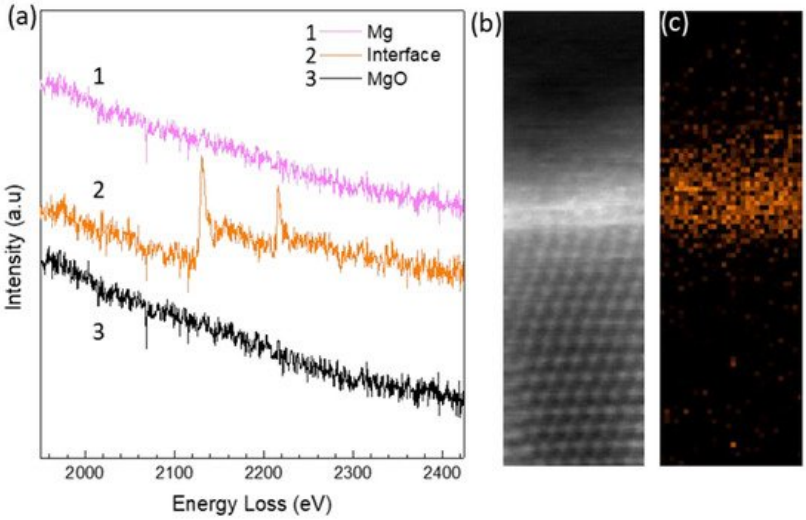

Figure 27. Yttrium segregation at Mg/(1 1 1)MgO interface [40]. (**a**) STEM/EELS spectra acquired from areas of Mg (curve 1), MgO/Mg interface (curve 2) and MgO (curve 3) where yttrium edge loss is clearly seen from curve 2; (**b**) STEM HAADF image along [0 1 1]MgO direction during EELS acquisition; and (**c**) corresponding EELS elemental map of yttrium, showing segregation of yttrium at the interface.

High resolution STEM HAADF images in **Figure 28**a,b show the Mg/{1 1 1}MgO interface observed in $[2\ 1^{-}\ 1]_{MgO}$ and $[0\ 1\ 1]_{MgO}$ directions, respectively. There are two interfacial atomic layers in which the atomic columns exhibit a higher brightness than (Mg, O) columns of MgO (O columns are invisible) in the HAADF images, verifying the presence of Y atoms in the two layers. Extensive STEM/EELS revealed that O atoms were also involved in the segregation region and an O layer was located between the two Y-containing layers [40][56]. In terms of both the structure and chemistry, it was found that the 3 segregation layers, i.e., two Y layers and one O layer in between, resembled the three {1 0 0} layers of an fcc Y_2O_3 unit cell, although the measured spacing 2.73 Å between the two Y layers was slightly larger than 2.632 Å [57], the d-spacing of $\{2\ 0\ 0\}_{Y2O3}$ planes indicating that interfacial segregation of Y atoms from alloy melt led to the formation of Y_2O_3 2DC. **Figure 28**c,d illustrate schematically the atomic configuration of the segregated Y atoms viewed from $[2\ 1^{-}1]_{MgO}$ direction and 3D construction of the Y_2O_3 2-dimensional compound (2DC) at the interface.

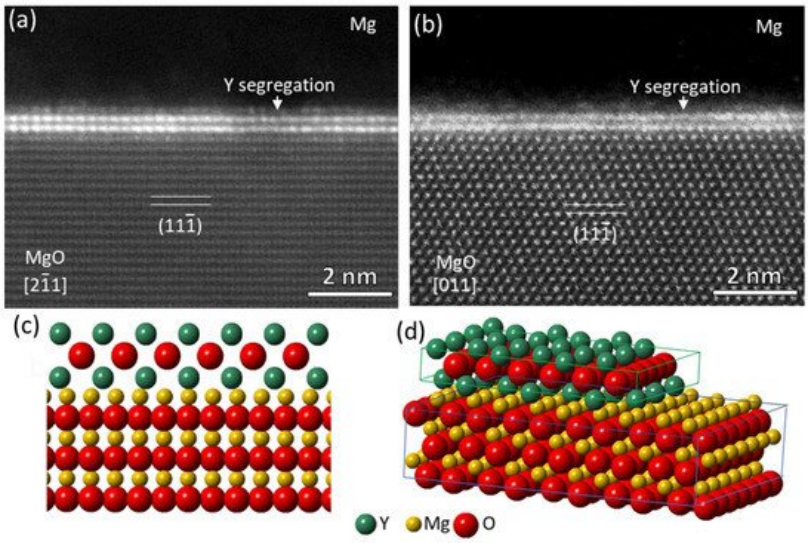

Figure 28. Nature of Y segregation layer at Mg/(1 1 1)MgO interface [40]. (**a**,**b**) High resolution STEM HAADF images showing interface between Mg and (1 1 1)MgO particle along (**a**) $[2\ 1^{-}1]$ MgO and (**b**) [0 1 1]MgO direction respectively, where two Y-containing atomic layers with a brighter contrast are visible; and (**c**,**d**) schematics showing (**c**) segregated Y atoms viewed from $[2\ 1^{-}1]$MgO direction and (**d**) 3D construction of Y_2O_3 2DC segregation layer.

With the formation of Y_2O_3 2DC at the Mg/(1 1 1) MgO interface, Mg nucleates on the Y_2O_3 2DC, instead of on the (1 1 1)MgO surface. The lattice misfit at the interface is, therefore, calculated as 1.71%, much smaller than the initial value of 7.9% between Mg and MgO, according to the OR5 below [40]:

$$\mathrm{OR}\,5:\ (0\,0\,2)\,[1\,0\,0]\mathrm{Y_2O_3} - 2\mathrm{DC}\ //(0\,0\,0\,2)\,[1\,0\,\bar{1}\,0]\,\mathrm{Mg}.$$

The much-reduced lattice misfit between Y_2O_3 2DC and Mg indicates an increased nucleation potency for MgO substrate with the Y segregation. In addition, the heat of mixing between Y and Mg was reported as ~6 kJ/mol [58], suggesting a strong affinity between Y and Mg atoms. A promotion of prenucleation is, therefore, expected in the melt close to the Mg melt/Y_2O_3-2DC interface due to the potential chemical reaction between Mg and Y atoms, subsequently promoting nucleation potency.

3.5. Y Segregation at Mg/MgO{1 0 0} Interface

Y segregation is also observed on the surface of {1 0 0} surface of cubic MgO particles in Mg-0.5Y melt. However, the behaviour of Y segregation on the {1 0 0} MgO surface is considerably different from that on the {1 1 1} MgO surface [40]. From $[0\ 0\ 1]_{MgO}$ and $[0\ 1\ 1]_{MgO}$ directions, respectively, the STEM HAADF images in **Figure 29** show that the atomic columns in an atomic monolayer at the Mg/(1 0 0)MgO interface have a high bright contrast, indicating that Y atoms are in the atomic layer. When viewed in $[0\ 0\ 1]_{MgO}$, Y-containing atomic columns are seen in every other (Mg, O) column of the top (1 0 0)MgO plane, resulting in the periodic brightness pattern, i.e., the brighter column appearing on every other column when viewed from [0 0 1]MgO direction, as shown in **Figure 29**a. The brightness pattern of the monolayer disappears when viewed from the [0 1 1]MgO direction, as shown in **Figure 29**b. This indicates that Y atoms are present only in the Mg columns of the top (1 0 0)MgO layer.

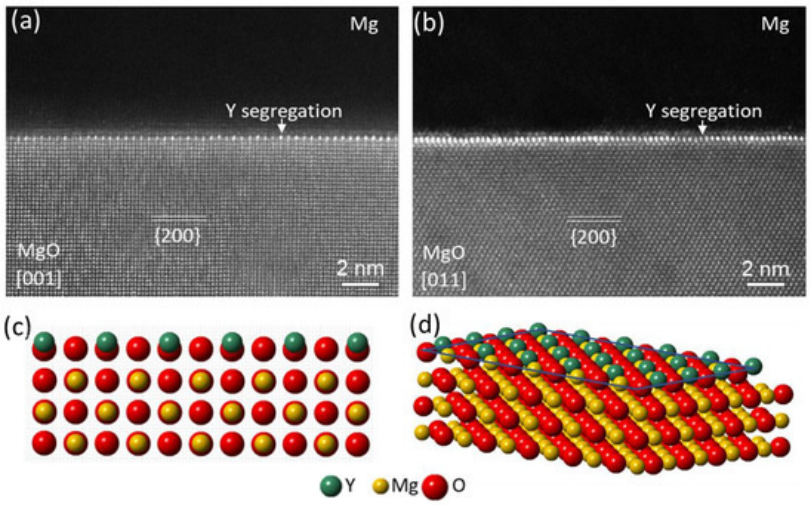

Figure 29. Nature of Y segregation layer at Mg/(1 0 0)MgO interface [40]. (**a**,**b**) High-resolution STEM HAADF images of (1 0 0)Mg/MgO interface viewed along (**a**) [0 0 1]MgO and (**b**) [0 1 1]MgO direction respectively, showing a bright atomic monolayer at the interface; and (**c**,**d**) schematics showing (**c**) segregated Y atoms viewed from [0 0 1] MgO direction and (**d**) 3D construction of the Y-containing monolayer on (1 0 0) surface of MgO.

It was also noted that the Y-containing atomic columns of the monolayer were elongated vertically when viewed from both [0 0 1]MgO and [0 1 1]MgO directions, with the protrusion being experimentally measured as 0.62 Å [40]. Further analysis showed that this was because only part of the Mg atoms in the columns of the top (1 0 0) MgO layer were substituted by Y atoms, with the Y atoms being protruded relative to the remaining Mg alloys in the column [40]. **Figure 29**c,d are schematics, showing the atomic configuration of the segregated Y atoms viewed from the [0 0 1] MgO direction and 3D construction of the monolayer on the (1 0 0) surface of MgO.

The Y-containing atomic monolayer on the {1 0 0} facets of the cubic MgO was coherent with the top {1 0 0}Mg plane, and, therefore, the lattice misfit between the newly formed monolayer and Mg remained the same as before. However, an atomic roughness was introduced to the monolayer due to the vertical protrusion by 0.62 Å of the Y atoms, which reduced the nucleation potency of the {1 0 0} cubic MgO and, thus, impeded prenucleation [9][55].

3.6. Segregation of Ca and Sn at Mg/MgO Interface

As one of the essential alloying elements in advanced high-performance Mg alloys, Ca is found to segregate readily at the Mg/MgO interface of native MgO particles. **Figure 30** shows the evidence of Ca segregation, where a layer about 1 nm thick is seen at the Mg/(1 1 1)MgO interface, appearing in a relatively lower contrast compared with MgO in the HAADF image in **Figure 30**a. STEM/EELS acquired from different positions across the interface in **Figure 30**b,c indicate that the chemistry of the segregation layer differs from that of MgO or Mg matrix. Ca segregation at the Mg/MgO interface is associated with N which comes from the protection atmosphere during casting process. Detailed analyses showed [50][56]

that the Ca segregation layer at Mg/MgO particles had a crystal structure resembling that of the bulk MgO crystal, with Ca and N atoms selectively substituting some of the Mg and O atoms on the MgO surface, respectively. The co-segregation of Ca and N results in a surface roughness and in-plane disordering, which, in turn, makes the pre-nucleation difficult, reducing nucleation potency of the MgO modified by the co-segregation of Ca and N.

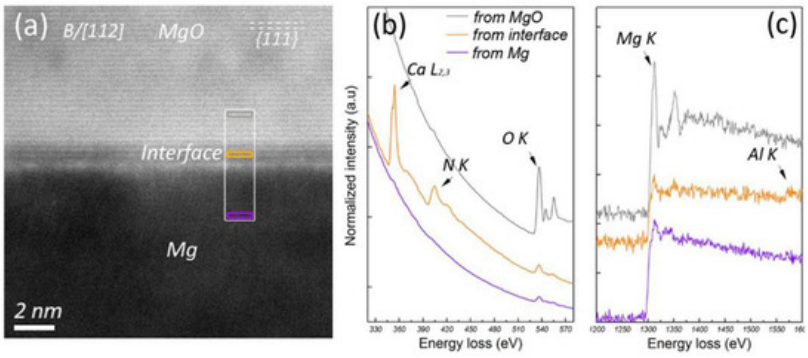

Figure 30. Ca segregation at Mg/(1 1 1)MgO interface [50][56]. (**a**) STEM-HAADF image of interface between Mg and MgO, showing a segregation layer at the interface; (**b**,**c**) EELS spectra acquired from different areas across the interface as indicated in the HAADF image.

Figure 31 gives evidence of Sn segregation at the Mg/(1 0 0)MgO interface. The HAADF images in **Figure 31**a,b show that there is a layer with a brighter contrast at the interface, apparently indicating an enrichment in Sn at the interface. The EELS in **Figure 31**c,d confirms the Sn segregation. It is shown that the segregated Sn atoms selectively substitute some of the Mg atoms in MgO without changing the lattice structure [56]. Detailed chemical and structural revealed that, with Sn segregation at the Mg/MgO interface, a roughness on the atomic scale was introduced and, thus, the ability for Mg to pre-nucleate on the MgO particles decreased [56].

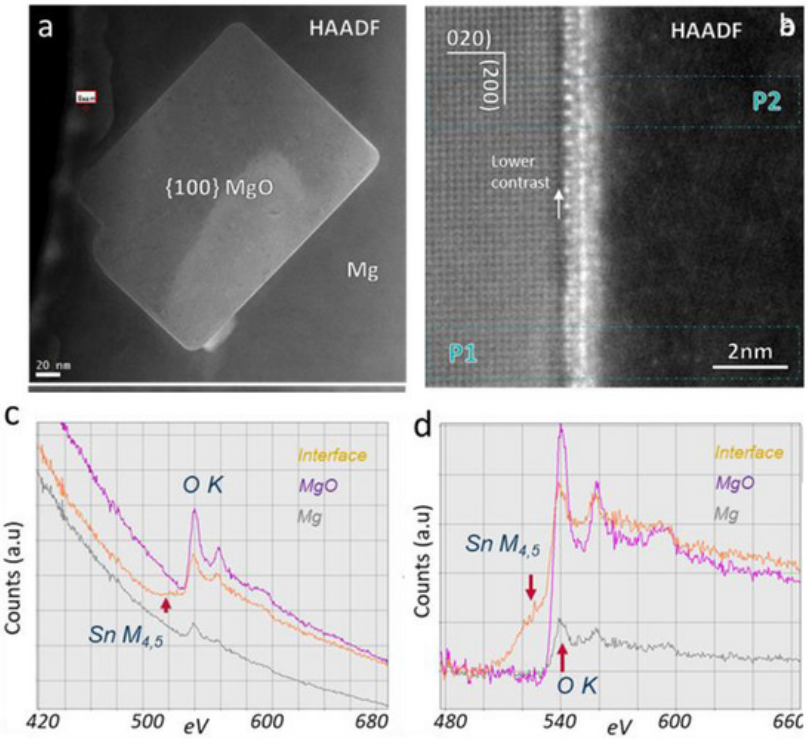

Figure 31. Sn segregation at Mg/(1 0 0)Mg interface [56]. (**a**,**b**) STEM HAADF images showing (**a**) general view of a {1 0 0} cubic MgO and (**b**) the Mg/MgO interface viewed in [0 0 1]MgO direction; and (**c**,**d**) the EELS spectra without and with background subtraction suggesting that Sn exists at the interface (indicated by the arrows).

4. Segregation at Al/γ-Al_2O_3 Interface

4.1. Nature of γ-Al_2O_3

Liquid Al oxidizes readily at the surface when it is exposed to an atmosphere containing oxygen and/or water moisture, producing two major types of alumina, γ-Al_2O_3 and α-Al_2O_3, with different crystal structures. The alumina is subjected to transformation from γ-Al_2O_3 to α-Al_2O_3 with increasing time and temperature. The formation of α-Al_2O_3 was reported to

occur at temperatures higher than 850 °C in Al-alloy melts [59]. Over the temperature range involved for cast processing of Al-alloys, typically lower than 750~800 °C, the native alumina formed in the melts are γ-Al_2O_3 [48][60][61][62][63]. However, Mg addition to Al alloys results in change of the oxide from Al_2O_3 to $MgAl_2O_4$ spinel or MgO, depending on Mg concentration [48][60][63]. The alumina in commercially pure Al (CP-Al) at 750 °C are usually in the form of films (**Figure 32**a) containing enormous individual γ-Al_2O_3 particles (**Figure 32**b). Typically, γ-Al_2O_3 particles in CP-Al melt display platelet-like morphology, about 50 nm thick and 200–300 nm long on average (**Figure 33**a). {1 1 1} crystal planes are the terminating surfaces of the faceted alumina platelets, and twins along the {1 1 1} planes are also frequently observed inside them (**Figure 33**b). For convenience, γ-Al_2O_3 with a {1 1 1} faceted morphology is denoted as γ-Al_2O_3{1 1 1}.

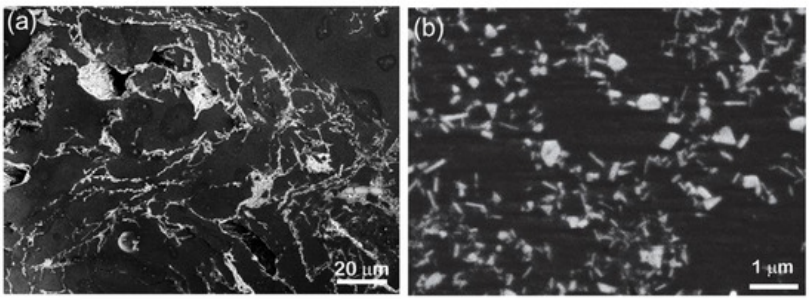

Figure 32. Morphology of native γ-Al_2O_3 films/particles in CP-Al [48][60]. SEM micrographs showing the general view of (**a**) γ-Al_2O_3 films at low magnification and (**b**) the discrete γ-Al_2O_3 particles collected from commercial purity Al (CP-Al) at 750 °C by melt filtration.

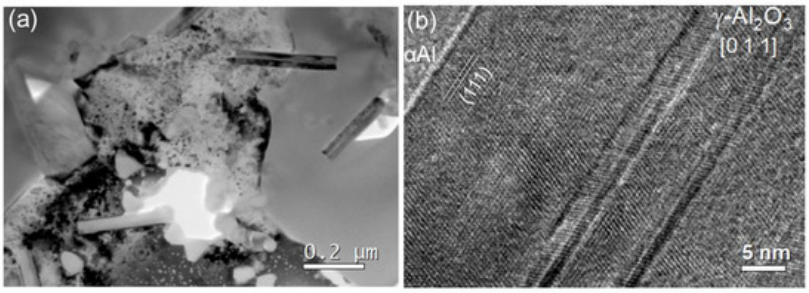

Figure 33. Faceted behavior of the native γ-Al_2O_3 particles in CP-Al melt [48][60]. TEM micrograph showing (**a**) the typical morphology of the faceted γ-Al_2O_3 particles in commercial purity Al (CP-Al) melt, which display a platelet-like morphology about 50 nm thick and 200–300 nm long on an average; and (**b**) high resolution TEM micrograph showing the γ-Al_2O_3 particle is faceted and twinned along its {1 1 1} planes.

4.2. Y Segregation at Al/γ-Al_2O_3 Interface

Al_2O_3 particles were collected from Al-0.075Y alloy melt and segregation of Y at the interface between Al and {1 1 1} terminating surface of γ-Al_2O_3 was investigated. The experimental results revealed the evidence of Y segregation at the Al/γ-Al_2O_3 interface, which was consistently observed by high resolution STEM-HAADF/ADF images, STEM/EDS mapping and STEM/EELS analysis, etc. **Figure 34**a is a Z-contrast STEM-HAADF image of Al/γ-Al_2O_3 interface, where a monolayer with a brighter contrast than the γ-Al_2O_3 is observed. The yttrium atom was much heavier than Al (Z_Y = 39 vs. Z_{Al} = 13), so the brighter contrast in the HAADF image suggests Y enrichment in the monolayer at the interface. The arrangement of Y-rich atomic columns in the monolayer was identical to the high-density Al columns in the γ-Al_2O_3 crystal, having an interatomic spacing of ½ < 011 > $_{\gamma\text{-}Al2O3}$. The Y segregation layer was found to cover the whole Al/γ-Al_2O_3 interface, confirmed by the STEM/EDS mapping in **Figure 34**b–d.

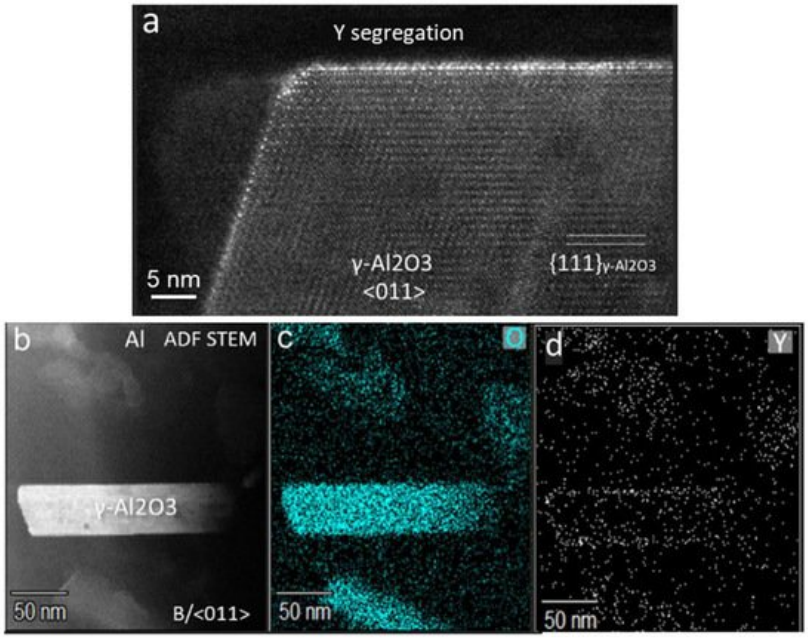

Figure 34. Y segregation at Al/γ-Al_2O_3 interface. (**a**) STEM-HAADF image of Al/γ-Al_2O_3 interface for a γ-Al_2O_3 particle in Al-0.075Y alloy; (**b**) STEM ADF image; and EDS elemental mapping of (**c**) O and (**d**) Y, showing Y enrichment at the interface.

Ab initio molecular dynamics (AIMD) simulation was performed to clarify the above experimental evidence of Y interfacial segregation and to reveal the effect of segregation on the atomic ordering of liquid atoms close to the L-Al/γ-Al_2O_3{1 1 1} interfaces. As shown in **Figure 35**a,b, Y atoms (large dark green spheres) in Al melt tend to segregate at the L-Al/γ-Al_2O_3{1 1 1} interface, due to their lower electronegativity values than Al and higher stability of yttria than that of alumina. Both structurally and chemically, Y segregation results in the formation of approximately Al_2Y two-dimensional compound (2DC) and the reconstruction of the metal layers adjacent to the surface of the γ-Al_2O_3{1 1 1} substrate, in agreement with the HR-STEM results. It was also seen from the atomic density profiles in **Figure 35**c,d that the segregated Y atoms protruded into the alloy melt with respect to the Al atoms, and this splitting of the terminating layer would introduce an atomic roughness to the {1 1 1} surface of the γ-Al_2O_3. As a consequence, the potency of the γ-Al_2O_3 substrate for nucleation of Al was weakened. **Figure 35**e,f show the top view of the in-plane atomic arrangement of the Y segregation layer at the Al/γ-Al_2O_3 interface, showing the atomic arrangement of the Al_2Y 2DC.

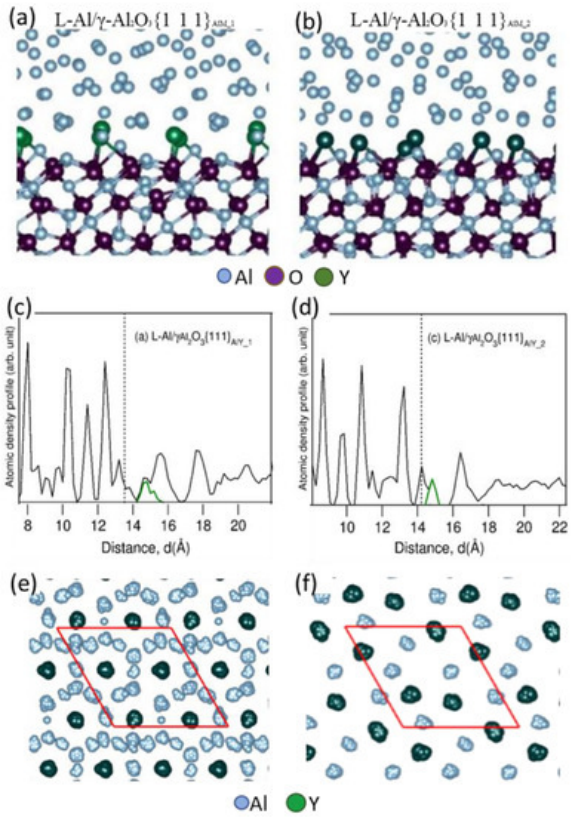

Figure 35. Ab initio molecular dynamics (AIMD) simulation of Y segregation at L-Al/γ-Al_2O_3 interface. (**a**,**b**) Snapshots of Y segregation at (**a**) L-Al/γ-$Al_2O_3$$\{1\ 1\ 1\}_{AIM_1}$ and (**b**) L-Al/γ-$Al_2O_3$$\{1\ 1\ 1\}_{AIM_2}$ interfaces at equilibrium at 1000 K; (**c**,**d**) atomic density profiles ρ(z) of Y segregated at the L-Al/γ-$Al_2O_3$$\{1\ 1\ 1\}_{AIM}$ interfaces where the black curve represents ρ(z) for all atoms, while the dark-green curve is for Y; and (**e**,**f**) top view of in-plane atomic arrangement of the Y segregation layer at the L-Al/γ-$Al_2O_3$$\{1\ 1\ 1\}_{AIM}$ interfaces. The blue spheres represent Al atoms, dark-brown O, and dark-green Y.

4.3. La Segregation at Al/γ-Al_2O_3 Interface

La segregation was readily observed at Al/γ-Al_2O_3 interfaces during the examination of multiple numbers of γ-Al_2O_3 particles in Al-0.075La and Al-0.75La alloys [62]. **Figure 36** shows a STEM-HAADF/ADF image and STEM/EDS maps covering a γ-Al_2O_3 particle from Al-0.75La alloy melt, where a brighter monolayer at the interface is clearly visible, with the brighter atomic columns in the monolayer arranged in an interatomic spacing of ½ < 0 1 1 > $_{\gamma\text{-}Al2O3}$. The existence of La in the bright atomic columns of the monolayer was further confirmed by the EDS map of La in **Figure 36**d, where La segregation was seen to continuously cover the Al/γ-Al_2O_3 interface.

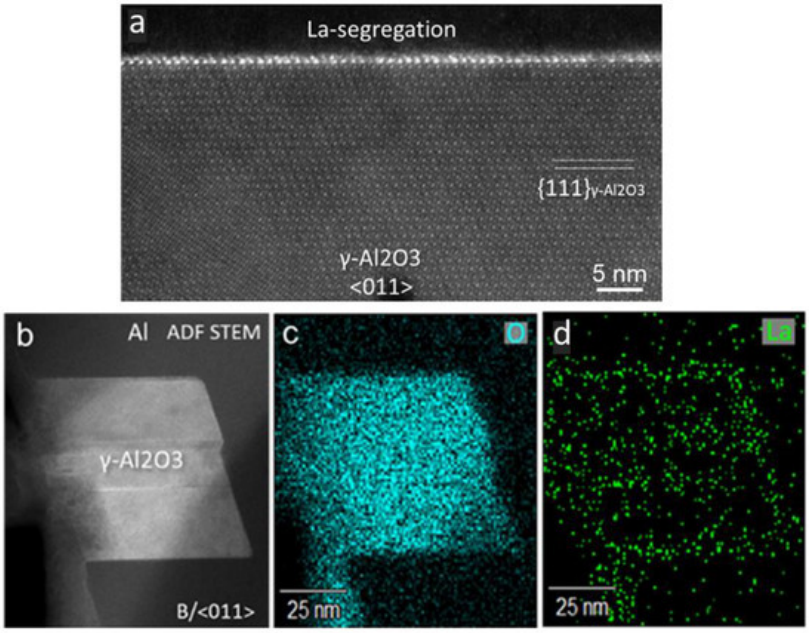

Figure 36. La segregation at Al/γ-Al_2O_3 interface [62]. (**a**) STEM Z-contrast HAADF image of Al/γ-Al_2O_3 interface for a γ-Al_2O_3 particle in Al-0.75La alloy; (**b**) STEM ADF image; and (**c**,**d**) EDS elemental mapping of (**c**) O, (**d**) La, showing La enrichment at the interface.

AIMD simulation of the L-Al/γ-Al_2O_3 interface where La segregated showed similar results to that of the interface with Y segregation [62]. As shown in **Figure 37**, La atoms (light-green spheres) were found to segregate at the interface, with the structure and chemistry of the La-containing layer being similar to Al_2La 2DC. In addition, the La atoms with a much larger atomic radius than Al atoms were seen to protrude into the alloy melt, as shown in **Figure 37**a,b. The protrusion of La atoms is clearly seen in the atomic density profiles in **Figure 37**c,d. **Figure 37**e,f show the top view of the in-plane atomic arrangement of the La segregation layer at the Al/γ-Al_2O_3 interface, indicating the formation of Al_2Y 2DC. Due to the protrusion of La atoms in the Al_2La 2DC layer at the interface, the γ-Al_2O_3 surface was atomically rough. The simulation revealed that, due to the atomic roughness of the Al_2O_3 surface, the prenucleation at the L-Al/γ-$Al_2O_3$$\{1\ 1\ 1\}$ interface was weakened to a similar level by the interfacial segregation of Y and La atoms.

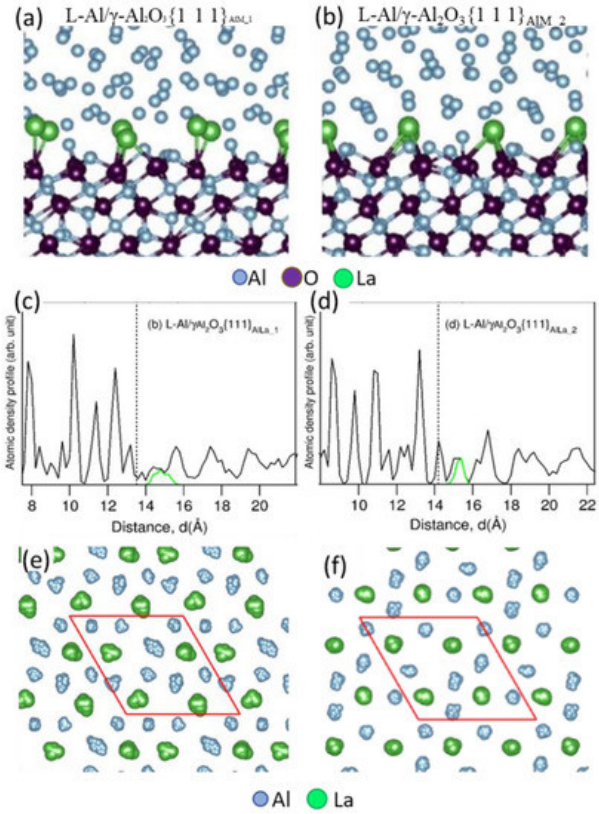

Figure 37. Ab initio molecular dynamics (AIMD) simulation of La segregation at L-Al/γ-Al_2O_3 interface [62]. (**a**,**b**) Snapshots of La segregation at (**a**) L-Al/γ-$Al_2O_3$$\{1\ 1\ 1\}_{AIM_1}$ and (**b**) L-Al/γ-$Al_2O_3$$\{1\ 1\ 1\}_{AIM_2}$ interfaces at equilibrium at 1000 K; (**c**,**d**) atomic density profiles ρ(z) of La segregated at the L-Al/γ-$Al_2O_3$$\{1\ 1\ 1\}_{AIM}$ interfaces where the black curve represents ρ(z) for all atoms, while the light-green curve is for La; and (**e**,**f**) top view of in-plane atomic arrangement of the La segregation layer at the L-Al/γ-$Al_2O_3$$\{1\ 1\ 1\}_{AIM}$ interfaces. The blue spheres represent Al atoms, dark-brown O, and light-green La.

References

1. McCartney, D.G. Grain refining of aluminium and its alloys using inoculants. Int. Mater. Rev. 1989, 34, 247–260.
2. Murty, B.S.; Kori, S.A.; Chakraborty, M. Grain refinement of aluminium and its alloys by heterogeneous nucleation and alloying. Int. Mater. Rev. 2002, 47, 3–47.
3. Easton, M.A.; Qian, M.; Prasad, A.; StJohn, D.H. Recent advances in grain refinement of light metals and alloys. Curr. Opin. Solid State Mater. Sci. 2016, 20, 13–24.
4. Quested, T.E. Understanding mechanisms of grain refinement of aluminium alloys by inoculation. Mater. Sci. Technol. 2004, 20, 1357–1369.
5. Greer, L. Overview: Application of heterogeneous nucleation in grain-refining of metals. J. Chem. Phys. 2016, 145, 211704.
6. StJohn, D.H.; Qian, M.; Easton, M.A.; Cao, P.; Hildebrand, Z. Grain refinement of magnesium alloys. Metall. Mater. Trans. A 2005, 36A, 1669–1679.
7. StJohn, D.H.; Easton, M.A.; Qian, M.; Taylor, J.A. Grain refinement of magnesium alloys: A review of recent research, theoretical developments, and their application. Metall. Mater. Trans. A 2013, 44, 2935–2949.
8. Fan, Z. An epitaxial model for heterogeneous nucleation on potent substrates. Metall. Mater. Trans. A 2013, 44, 1409–1418.
9. Jiang, B.; Men, H.; Fan, Z. Atomic ordering in the liquid adjacent to an atomically rough solid surface. Comp. Mater. Sci. 2018, 153, 73–81.
10. Fang, C.M.; Men, H.; Fan, Z. Effect of substrate chemistry on prenucleation. Metall. Mater. Trans. A 2018, 49, 6231–6242.
11. Fan, Z.; Wang, Y.; Zhang, Y.; Qin, T.; Zhou, X.; Thompson, G.E.; Pennycook, T.; Hashimoto, T. Grain refining mechanism in the Al/Al-Ti-B system. Acta Mater. 2015, 84, 292–304.
12. Wang, Y.; Petal, J.B.; Zhang, Y.; Fan, Z. Examination of Commercial Al-5Ti-1B Grain Refiners from MQP Ltd and STNM Ltd, Technical Report; MQP Ltd: Solihull, UK, 2021.

13. Fan, Z.; Men, H.; Wang, Y.; Que, Z.P. A new atomistic mechanism for heterogeneous nucleation in the systems with negative lattice misfit: Creating a 2D template for crystal growth. Metals 2021, 11, 478.

14. Greer, A.L.; Bunn, A.M.; Tronche, A.; Evans, P.V.; Bristow, D.J. Modelling of inoculation of metallic melts: Application to grain refinement of aluminium by Al-Ti-B. Acta Mater. 2000, 48, 2823–2835.

15. Qin, T.; Fan, Z. Molecular analysis of grain refining in aluminium with Al-5Ti-B. IOP Conf. Ser. Mater. Sci. Eng. 2011, 27, 012007.

16. Wang, J.; Horsfield, A.; Schwingenschlögl, U.; Lee, P.D. Heterogeneous nucleation of solid Al from the melt by TiB2 and Al3Ti: An ab initio molecular dynamics study. Phys. Rev. B 2010, 82, 184203.

17. Ma, S.; Yan, R.; Jing, T.; Dong, H. Substrate-induced liquid layering: A new insight into the heterogeneous nucleation of liquid metals. Metals 2018, 8, 521.

18. Men, H.; Fan, Z. An analytical model for solute segregation at liquid metal/solid substrate interface. Metall. Mater. Trans. A 2014, 45, 5508–5516.

19. Jones, G.P.; Pearson, J. Factors affecting the grain-refinement of aluminium using titanium and boron additives. Metall. Trans. B 1976, 7, 223–234.

20. Birch, M.E.J.; Fisher, P. Grain refining of commercial aluminium alloys with titanium boron aluminium. In Aluminium Technology ’86: Proceedings of the International Conference; Shepard, T., Ed.; The Institute of Metals: London, UK, 1986; pp. 117–124.

21. Ahmady, S.M.; McCartney, D.G.; Thistlethwaite, S.R. Assessment of aluminium grain refiner performance using the ALCOA test. In Light Metals 1990; Bickert, C.M., Ed.; TMS: Warrendale, PA, USA, 1990; pp. 837–843.

22. Kearns, M.A.; Cooper, P. Effects of solutes on grain refinement of selected wrought aluminium alloys. Mater. Sci. Technol. 1997, 13, 650–654.

23. Birch, M.E.J.; Cowell, A.J.J. Grain refinement of aluminium alloys containing chromium and zirconium. In Solidification Processing 1987; Beech, J., Jones, H., Eds.; The Institute of Metals: London, UK, 1988; pp. 149–152.

24. Abdel-Hamid, A.A. Effect of other elements on the grain refinement of Al by Ti or Ti and B. Part I—A critical review. Z. Metallkd. 1989, 80, 566–569.

25. Abdel-Hamid, A.A. Effect of other elements on the grain refinement of aluminum by titanium or titanium and boron. Part II. Effect of the refractory metals vanadium, molybdenum, zirconium, and tantalum. Z. Metallkd. 1989, 80, 643–647.

26. Wang, Y.; Fang, C.M.; Zhou, L.; Hashimoto, T.; Zhou, X.; Ramasse, Q.M.; Fan, Z. Mechanism for Zr poisoning of Al-Ti-B based grain refiners. Acta Mater. 2019, 164, 428–439.

27. Wang, Y.; Zhou, L.; Fan, Z. Mechanism of zirconium poisoning effect on TiB2 inoculation in aluminium alloys. In Light Metals 2016; Williams, E., Ed.; TMS: Warrendale, PA, USA, 2016; pp. 725–729.

28. Koch, C. Determination of Core Structure Periodicity and Point Defect Density Along Dislocations. Ph.D. Thesis, Arizona State University, Tempe, AR, USA, January 2002.

29. Dolukhanyan, S.K.; Aleksanyan, A.G.; Ter-Galstyan, O.P.; Shekhtman, V.S.; Sakharov, M.K.; Abrosimova, G.E. Specifics of the formation of alloys and their hydrides in Ti-Zr-H system. Russ. J. Phys. Chem. B 2007, 1, 563–569.

30. Khaliq, A.; Rhamdhani, M.A.; Brooks, G.A.; Grandfield, J. Thermodynamic analysis of Ti, Zr, V and Cr impurities in aluminium melt. In Light Metals 2011; Lindsay, S.J., Ed.; TMS: Warrendale, PA, USA, 2011; pp. 751–756.

31. Farrar, P.A.; Adler, S. On the system titanium-zirconium. Trans. Metall. Soc. AIME 1996, 236, 1061–1064.

32. Men, H.; Fan, Z. Prenucleation induced by crystalline substrates. Metall. Mater. Trans. A 2018, 49, 2766–2777.

33. Wang, Y.; Que, Z.P.; Hashimoto, T.; Zhou, X.; Fan, Z. Mechanism for Si poisoning of Al-Ti-B grain refiners in Al alloys. Metall. Mater. Trans. A 2020, 51, 5743–5757.

34. Que, Z.P.; Zhou, Y.P.; Xia, J.H.; Wang, Y.; Fang, C.M.; Mendis, C.L.; Fan, Z. Heterogeneous nucleation and refinement of Fe-containing intermetallic compounds in Al alloys. In The Future Liquid Metal Engineering Hub, Report 2015–2021; LiME: Uxbridge, UK, 2021; pp. 44–45. Available online: https://www.lime.ac.uk/blog/2021-annual-report-published (accessed on 1 October 2021).

35. Que, Z.P.; Wang, Y.; Mendis, C.L.; Fang, C.M.; Xia, J.H.; Zhou, X.R.; Fan, Z. Formation, morphology control and refinement of Fe-containing intermetallic compounds in Al alloys: An overview. Metals, 2022; in press.

36. Que, Z.P.; Zhou, Y.P.; Wang, Y.; Fan, Z. Composition templating for heterogeneous nucleation of intermetallic compounds. In SP’17-Solidification Processing 2017; Fan, Z., Ed.; Brunel University London: Uxbridge, UK, 2017; pp. 158–161.

37. Que, Z.; Wang, Y.; Fan, Z. Heterogeneous nucleation of eutectic structure in Al-Mg-Si alloys. Metall. Mater. Trans. A 2020, 51, 2697–2702.

38. Fan, Z.; Que, Z.; Wang, Y.; Jiang, B. Structural and compositional templating for heterogeneous nucleation. In Frontiers in Sonification; Kurz, W., Dantzig, J., Karma, A., Hoyt, J., Eds.; Symposium in honour of Michel Rappaz; TMS: Warrendale, PA, USA, 2016; pp. 17–21.

39. Li, J.; Hage, F.S.; Ramasse, Q.M.; Schumacher, P. The nucleation sequence of α-Al on TiB2 particles in Al-Cu alloys. Acta Mater. 2021, 206, 116652.

40. Wang, S.H.; Wang, Y.; Ramasse, Q.M.; Schmid-Fetzer, R.; Fan, Z. Segregation of yttrium at Mg/MgO interface in Mg-Y alloy. Acta Mater. 2022.

41. Fan, Z.; Wang, Y.; Xia, M.; Arumuganathar, S. Enhanced heterogeneous nucleation in AZ91D alloy by intensive melt shearing. Acta Mater. 2009, 57, 4891–4901.

42. Wang, Y.; Fan, Z.; Zhou, X.; Thompson, G.E. Characterisation of magnesium oxide and its interface with α-Mg in Mg-Al based alloys. Phil. Mag. Lett. 2011, 91, 516–529.

43. Wang, S.H.; Wang, Y.; Ramasse, Q.; Fan, Z. The nature of native MgO in Mg and its alloys. Metall. Mater. Trans. A 2020, 51, 2957–2974.

44. Wang, Y.; Peng, G.S.; Fan, Z. Grain refinement of Mg and its alloys by inoculation of in situ MgO particles. In Magnesium Technology 2017; Solanki, K.N., Orlov, D., Singh, A., Neelameggham, N.R., Eds.; TMS: Warrendale, PA, USA, 2017; pp. 99–106.

45. Fan, Z.; Wang, Y.; Zhang, Z.F.; Xia, M.; Li, H.T.; Xu, J.; Granasy, L.; Scamans, G.M. Shear enhanced heterogeneous nucleation in some Mg- and Al- alloys. Int. J Cast Metals Res. 2009, 22, 318–322.

46. Wang, Y.; Xia, M.; Fan, Z.; Zhou, X.; Thompson, G.E. The effect of Al8Mn5 intermetallic particles on grain size of as-cast Mg-Al-Zn AZ91D alloy. Intermetallics 2010, 18, 1683–1689.

47. Fan, Z.; Gao, F.; Wang, Y.; Wang, S.H.; Petal, J.B. Grain refining of Mg-alloys by native MgO particles: An overview. J. Magnes. Alloy. 2022; in press.

48. Wang, Y.; Li, H.T.; Fan, Z. Grain refinement of Al- and Mg- alloys by native oxide particles. In Solidification Processing 2017; Fan, Z., Ed.; Brunel University London: Uxbridge, UK, 2017; pp. 81–86.

49. Peng, G.S.; Wang, Y.; Fan, Z. Competitive heterogeneous nucleation between Zr and MgO particles in commercial purity magnesium. Metall. Mater. Trans. A 2018, 49, 2182–2192.

50. Wang, S.H.; Wang, F.; Wang, Y.; Ramasse, Q.M.; Fan, Z. Segregation of Ca at the Mg/MgO interface and its effect on grain refinement of Mg alloys. Mater. Sci. Eng. 2019, 529, 012048.

51. Zuo, Y.B.; Xia, M.X.; Liang, S.M.; Wang, Y.; Scamans, G.M.; Fan, Z. Grain refinement of DC cast AZ91D Mg alloy by intensive melt shearing. Mater. Sci. Technol. 2011, 27, 101–107.

52. Liu, G.; Wang, Y.; Fan, Z. A physical approach to the direct recycling of Mg-alloy scrap by the rheo-diecasting process. Mater. Sci. Eng. A 2008, 472, 251–257.

53. Fan, Z.; Gao, F.; Jiang, B.; Que, Z. Impeding nucleation for more significant grain refinement. Sci. Rep. 2020, 10, 9448.

54. Men, H.; Jiang, B.; Fan, Z. Mechanisms of grain refinement by intensive shearing of AZ91 alloy melt. Acta Mater. 2010, 58, 6526–6534.

55. Fang, C.M.; Fan, Z. Prenucleation at the interface between MgO and liquid magnesium: An ab initio molecular dynamics study. Metall. Mater. Trans. A 2020, 51, 788–797.

56. Wang, S.H. Characterisation of Native MgO and Its Roles in Solidification of Mg Alloys. Ph.D. Thesis, Brunel University London, London, UK, 2020.

57. Katagiri, S.; Ishizawa, N.; Marumo, F. A new high temperature modification of face-centered cubic Y2O3. Powder Diffr. 1993, 8, 60.

58. Takeuchi, A.; Inoue, A. Classification of bulk metallic glasses by atomic size difference, heat of mixing and period of constituent elements and its application to characterization of the main alloying element. Mater. Trans. 2005, 41, 846–2829.

59. Narayanan, L.A.; Samuel, F.H.; Gruzleski, J.E. Crystallization behaviour of iron-containing intermetallic compounds in 319 aluminium alloy. Metall. Mater. Trans. A 1994, 25, 1761–1773.

60. Wang, Y.; Li, H.T.; Fan, Z. Oxidation of aluminium alloy melts and inoculation by oxide particles. Trans. Indian Inst. Met. 2012, 65, 653–661.

61. Li, H.T.; Wang, Y.; Xia, M.; Zuo, Y.; Fan, Z. Harnessing oxides in liquid metals and alloys. In Solidification Science and Technology: Proceedings of the John Hunt International Symposium 12–14 December 2011, Brunel University, UK; Fan, Z., Stone, I.C., Eds.; Brunel University Press: Uxbridge, UK, 2011; pp. 93–110.
62. Wang, S.H.; Fang, C.M.; Wang, Y.; Lordan, E.; Fan, Z. Segregation of La at Al/γ-Al2O3 interface. Acta Mater. 2022; submitted.
63. Li, H.T.; Wang, Y.; Fan, Z. Mechanisms of heterogeneous nucleation during solidification in binary Al-Mg alloys. Acta Mater. 2012, 60, 1528–1537.